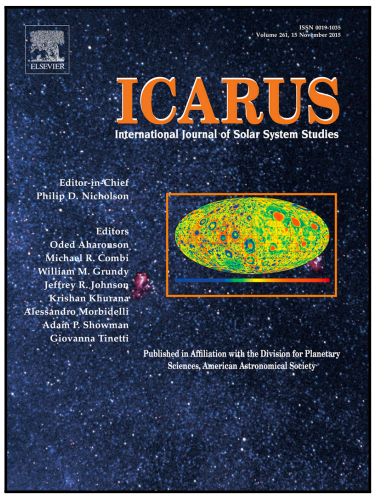

Lunar Floor-Fractured Craters: Modes of Dike and Sill Emplacement and Implications of Gas Production and Intrusion Cooling on Surface Morphology and Structure

Lionel Wilson , James W. Head

PII: S0019-1035(17)30622-X
DOI: 10.1016/j.icarus.2017.12.030
Reference: YICAR 12750

To appear in: *Icarus*

Received date: 30 August 2017
Revised date: 15 December 2017
Accepted date: 20 December 2017

Please cite this article as: Lionel Wilson , James W. Head , Lunar Floor-Fractured Craters: Modes of Dike and Sill Emplacement and Implications of Gas Production and Intrusion Cooling on Surface Morphology and Structure, *Icarus* (2017), doi: 10.1016/j.icarus.2017.12.030

Highlights

- We model the intrusion processes that result in lunar floor-fractured craters (FFCs).
- Dike initiates sill, causing floor uplift (hours); lateral sill extent controlled by wall load.
- Gas bubbles rise to sill top (decades), create foam layer and free gas layer above foam, causing further uplift up to ~30 m; eruptions possible.
- Late stage sill cooling (centuries) results in subsidence of up to ~350 m.
- These predictions provide a basis to test the theory from observations of individual FFCs.

Lunar Floor-Fractured Craters: Modes of Dike and Sill Emplacement and Implications of Gas Production and Intrusion Cooling on Surface Morphology and Structure

Lionel Wilson[1,2] **and James W. Head**[2]
[1]Lancaster Environment Centre, Lancaster University,
Lancaster LA1 4YQ, UK

[2]Department of Earth, Environmental and Planetary Sciences,
Brown University, Providence, RI 02912 USA

Abstract

Lunar floor-fractured craters (FFCs) represent the surface manifestation of a class of shallow crustal intrusions in which magma-filled cracks (dikes) rising to the surface from great depth encounter contrasts in host rock lithology (breccia lens, rigid solidified melt sheet) and intrude laterally to form a sill, laccolith or bysmalith, thereby uplifting and deforming the crater floor. Recent developments in the knowledge of lunar crustal thickness and density structure have enabled important revisions to models of the generation, ascent and eruption of magma, and new knowledge about the presence and behavior of magmatic volatiles has provided additional perspectives on shallow intrusion processes in FFCs. We use these new data to assess the processes that occur during dike and sill emplacement with particular emphasis on tracking the fate and migration of volatiles and their relation to candidate venting processes. FFCs result when dikes are capable of intruding close to the surface, but fail to erupt because of the substructure of their host impact craters, and instead intrude laterally after encountering a boundary where an increase in ductility (base of breccia lens) or rigidity (base of solidified melt sheet) occurs. Magma in dikes approaching the lunar surface experiences increasingly lower overburden pressures: this enhances CO gas formation and brings the magma into the realm of the low pressure release of H_2O and sulfur compounds, both factors adding volatiles to those already collected in the rising low-pressure part of the dike tip. High magma rise velocity is driven by the positive buoyancy of the magma in the part of the dike remaining in the mantle. The dike tip overshoots the interface and the consequent excess pressure at the interface drives the horizontal flow of magma to form the intrusion and raise the crater floor. If sill intrusion were controlled by the physical properties at the base of the melt sheet, dikes would be required to approach to within ~300 m of the surface, and thus eruptions, rather than intrusions, would be very likely to occur; instead, dynamical considerations strongly favor the sub-crustal breccia lens as the location of the physical property contrast localizing lateral intrusion, at a depth of several kilometers. The end of lateral and vertical sill growth occurs when the internal magma pressure equals the external pressure (the intrusion just supports the weight of the overlying crust). Dynamical considerations lead to the conclusion that dike magma volumes are up to ~1100 km^3, and are generally insufficient to form FFCs on the lunar farside; the estimated magma volumes available for injection into sills on the lunar nearside (up to ~800 km^3) are comparable to the observed floor uplift in many smaller FFCs, and thus consistent with these FFCs forming from a single dike emplacement event. In contrast, the thickest intrusions in the largest craters imply volumes requiring multiple dike contributions; these are likely to be events well-separated in time, rather than injection of new magma into a recently-formed and still-cooling intrusion.

We present a temporal sequence of 1) dike emplacement, 2) sill formation and surface deformation, 3) bubble rise, foam layer formation and collapse, 4) intrusion cooling, and a synthesis of predicted deformation sequence and eruption styles. Initial lateral injection of the sill at a depth well below the upper dike tip initiates upbowing of the overburden, leveraging deformation of the crater floor melt sheet above. This is followed by lateral spreading of the sill toward the edges of the crater floor, where crater wall and rim deposit overburden inhibit further lateral growth, and the sill grows vertically into a laccolith or bysmalith, uplifting the entire floor above the intrusion. Subsidiary dikes can be emplaced in the fractures at the uplift margins and will rise to the isostatic level of the initial dike tip; if these contain sufficient volatiles to decrease magma density, eruptions can also occur. This initial phase of intrusion, sill lateral spreading and floor uplift occurs within a few hours after initial dike emplacement. During the subsequent cooling of the sill, bubbles can rise hundreds of meters to the top of the intrusion to create a foam layer; when drainage of gas bubble wall magma occurs in the foam layer, a continuous gas layer forms above the foam. Gas formation and upward migration produces an increase in sill thickness, while subsequent cooling and solidification cause a thickness decreases and subsidence. The total topographic evolution history, following an initial 2 km thick sill intrusion and floor uplift (hours), includes further floor uplift by gas formation and migration (decades; ~30 m), followed by cooling, solidification and subsidence (~a century; ~350 m). An initial 2 km thick sill is predicted to have a final thickness of ~1.7 km. This predicted sequence of events can be compared with the sequence of floor deformation and volcanism in FFCs in order to test and refine this model.

I. Introduction and Background

Floor-fractured craters (FFCs - see Figure 1) are a distinctive class of lunar features, interpreted in the past to be the result of either viscous relaxation of impact craters (Masursky, 1964; Daneš, 1965; Cathles, 1975; Schultz, 1976; Hall et al., 1981; Wichman and Schultz, 1995; Dombard and Gillis, 2001) or magmatic intrusions into the breccia lenses beneath impact craters (Brennan, 1975; Schultz, 1976; Wichman and Schultz, 1995, 1996). Modern analyses strongly favor magmatic intrusion (Jozwiak et al., 2012; Thorey and Michaut, 2014; Jozwiak et al., 2015, 2017). There is an extensive literature on the formation of shallow sill, laccolith and bysmalith intrusions on Earth. Early suggestions that a sill forms when magma rising in a dike encounters a level of neutral buoyancy in the crust (Bradley, 1965; Roberts, 1970; Francis, 1982; Corry, 1988) are shown by later authors to be inconsistent with the interconnected vertical structure of many multiple sill complexes (Thomson, 2007; Menand, 2008, 2011), and the consensus is that neutral buoyancy is a contributor but not the controlling factor in initiating sills (Maccaferri et al., 2011). Instead, field evidence suggests that dikes are encouraged to initiate sill formation when they encounter a contrast in the host rock lithology (Johnson and Pollard, 1973, Pollard and Johnson, 1973; Thomson, 2007). Opinions differ greatly as to the relevance of ambient tectonic stresses, with advocates of the importance of tensional stresses at shallow depth (Gudmundsson, 2011) or of generally compressive tectonics (Maccaferri et al., 2011). Many authors suggest that sills should be initiated when dikes propagate through an interface where there is an increase in rigidity, i.e., shear modulus (Mathieu et al., 2008; Menand, 2008, 2011; Gudmundsson, 2011; Maccaferri et al., 2011; Schofield et al., 2012; Abdelmalak et al., 2012; Le Corvec et al., 2013).

This would clearly be relevant to dikes encountering impact melt sheets overlying breccias in impact craters. However, Schofield et al. (2012) also discuss the importance of host

rock rheology, citing field evidence (Pollard et al., 1975; Thomson, 2007; Schofield et al., 2010) and theoretical arguments for changes from brittle to non-brittle response in host rocks being a trigger for sill formation. The change from relatively unfractured crustal rocks beneath a crater to the base of a highly fractured and therefore ductile breccia lens, particularly on the Moon where processes such as hydrothermal alteration that might cement or lithify fractured rocks are absent, is therefore likely to be another favored location for sill injection. This idea is supported by the finding that 90% of FFCs occur in craters of Nectarian or younger age (Jozwiak et al., 2015). In general, the oldest, pre-Nectarian craters were formed in a warmer crust with a thinner lithosphere, encouraging thermal annealing of their breccia lenses. Dikes arriving beneath these craters later in lunar history would have found less contrast between the breccia lenses and the rocks beneath them than under younger craters. However, this simple picture is complicated by the observation from GRAIL data that gravity signatures linked to subsurface density anomalies, in part due to the presence of breccia lenses, show local correlations with crater size (Soderblom et al., 2015) superposed on global variations (Besserer et al., 2014), but not with crater age. Even so, this combination of age and hence thermal gradient controling on the conditions that encourage FFC formation may explain the observation that the early-formed major basins do not display floor-fracture characteristics: the catalog of Jozwiak et al. (2012) shows that 94% of all FFCs are less than 120 km in diameter, and the largest FFC is ~210 km in diameter. The same argument would suggest that the base of the highland mega-regolith would also not be a favored place for sill intrusions.

A final issue relates to terminology, specifically whether the intrusions under FFCs should be termed sills or laccoliths, or something else. The acceleration due to gravity, and hence the lithostatic pressure gradient in the interior, are smaller on the Moon than on Earth, and so the aspect ratios of all types of intrusion are expected to differ (Head and Wilson, 1992; Michaut, 2011; Thorey and Michaut, 2014; Wilson and Head, 2017a). Additional factors causing differences include the desiccated and impact-modified nature of the outer layers of the Moon mentioned above. For Earth, the consensus (Johnson and Pollard, 1973; Pollard and Johnson, 1973; Jackson and Pollard, 1988; Kerr and Pollard, 1998) is that sills are relatively thin and deform the rocks both above and below them elastically. If the sills spread far enough laterally, so that the overburden thickness is small compared with the horizontal extent of the intrusion, they deform the overlying rocks upward preferentially, becoming more nearly flat-floored and are then termed laccoliths. In some cases, failure occurs at the edges of the laccolith and wholesale uplift of the overburden occurs, with faulting at the edges of the uplifted block, producing a bysmalith. On the basis of applying these criteria to the lunar features, FFCs with significantly updomed floors, those of classes 2 and 4 in the catalog of Jozwiak et al. (2012), are underlain by laccoliths, whereas FFCs of classes 3 and 5, with much flatter uplifted floors, sit above bysmaliths. This interpretation is complicated, however, by the fact that many class 3 and 4 FFCs have a moat at the boundary between the floor and crater wall, a feature suggesting the marginal faulting expected for a bysmalith, whereas class 2 and 5 FFCs generally do not show this feature. Much of this complexity may be explained by the interaction between the diameter of the host crater and the injection rate of the magma that formed the intrusion (Thorey and Michaut, 2014). Since we are concerned mainly with processes that occur within an intrusion beneath an FFC after its emplacement, rather than with its morphological evolution during its emplacement, for simplicity we use the single term sill in this paper.

II. Analysis

Previous detailed treatments of the formation of FFCs by lateral intrusions beneath impact craters (Jozwiak et al., 2012; Thorey and Michaut, 2014; Jozwiak et al., 2015, 2017) have been based on the assumption that dikes approaching the lunar surface propagated from magma reservoirs in the lower crust or upper mantle and that these reservoirs were large enough that the source pressure remained at least approximately constant during the FFC formation event. However, recent work (Wilson and Head, 2017a; Head and Wilson, 2017) has shown that most lunar mare volcanism was probably driven by a different mechanism (Figure 2a). In this scenario, long-lived magma reservoirs in the crust and shallow mantle of the Moon are very rare; the majority of surface eruptions, and of shallow intrusions when these do happen, are fed by dikes originating deep in the mantle and reaching the surface with no intermediate storage stage. Deep in the mantle, the local stresses associated with the diapiric rise of a region of partial melt initiate a brittle fracture near the top of the partial melt zone - step (1) in Figure 2a. Melt percolates slowly into the fracture by buoyant flow between unmelted mineral grains. The fracture grows upward, forming a dike, until the stress distribution around it causes the base of the dike to pinch off from its source region, at which point the dike propagates as a discrete elastic structure containing a fixed volume at a finite excess pressure relative to its host rocks, the rocks above it fracturing and the rocks behind it closing as it travels upward (Weertman, 1971; Muller and Muller, 1980; Crawford and Stevenson, 1988) - step (2) in Figure 2a. The dike is buoyant in the mantle and rises until it reaches and penetrates the crust-mantle boundary - step (3). The magma in the dike is denser than the overlying crustal rocks and so the crust-mantle boundary represents a buoyancy trap for the dike magma. The dike attempts to reach equilibrium with its upper part in the crust and its lower part in the mantle. If the upper dike tip does not reach the surface there is no eruption, but an intrusion may form - step (4). However, if the dike has a great enough vertical extent, its upper tip will break through the surface and an eruption will ensue - step (5).

Whether or not an eruption occurs from a dike of a given size depends on the thickness of the crust, and GRAIL data show that the crust thickness is ~30 km on the nearside of the Moon and ~50 km on the farside (Wieczorek et al., 2013). The analysis of Wilson and Head (2017a, their Table 2) yields a range of values for the possible dike geometries and internal pressures that cause dikes to (a) fail to erupt anywhere on the Moon, (b) erupt through the nearside crust but not on the farside, and (c) erupt anywhere on the Moon. We associate FFCs with a sub-set of this range of options, viz., dikes that are capable of intruding close to the surface, whether on the nearside or the farside, but fail to erupt because of the structures they encounter beneath impact craters; instead they inject a sill laterally at some shallow depth. The successive steps in creating the intrusion are shown in detail in Figure 2b).

Two major phases are involved in the formation of an FFC. The first phase is the penetration of a dike into and through the crust until the upper dike tip enters the region beneath an impact crater and encounters conditions that encourage it to penetrate laterally instead of, or in addition to, continuing to penetrate vertically. As outlined above, these conditions could be an increase in ductility of the host rocks as the dike tip moves through the transition zone between intact crustal rocks and brecciated material beneath the crater, or an increase in rigidity as the dike tip penetrates into a solidified impact melt sheet on the crater floor. During this phase a vertical pressure gradient exists in the dike magma that reflects both the vertical weight of the magma and the pressure gradient driving the motion of the magma against friction with the walls of the dike. The stress intensities at the tips of dikes ascending from the lunar mantle are large and the propagation speeds of the dike tips, and of the magmas in the dikes, are also large,

thousands of MPa $m^{1/2}$ and tens of m s^{-1}, respectively (Wilson and Head, 2017a). For magma in a dike to flow into an incipient sill, the pressure in the magma at the level of the sill must be greater than the local lithostatic pressure, partly to initiate and then prop open the fracture that constitutes the sill, and partly to cause magma to flow into it. The width of the sill is initially very small, and as a result the speed of the magma flowing into the sill must also initially be small. This contrast between the vertical speed of magma in the dike and the initial horizontal speed of magma in the sill implies that the upper tips of dikes must always overshoot the levels at which lateral intrusions begin (Figure 2b).

The second FFC formation phase involves horizontal flow of magma from the dike into the sill within the sub-crater breccia while at the same time the part of the dike in the mantle is shrinking to feed the intrusion. The pressure distribution in the magma now changes continually, because only the shrinking vertical part of the system involves both the magma weight and the pressure gradient driving magma motion, and the only pressure gradient in magma flowing horizontally is that required to drive its motion against friction. This second phase terminates when magma stops moving and a static equilibrium is reached between the negatively buoyant magma in the upper part of the dike in the crust and the positively buoyant magma in the remaining lower part of the dike in the mantle. These two phases are now examined in detail.

A. Phase 1 - dike emplacement

To model this phase we require knowledge of the pressure gradient in the vertical part of the magma column in a propagating dike. This will be greater than the static weight of the magma, with the difference providing the gradient driving magma flow. The static weight will differ from the weight of an equivalent-length column of unvesiculated magma because the low pressure in the uppermost part of the dike will lead to gas exsolution and hence a reduction of the bulk density. Fortunately, these issues can be simplified, because values can be specified for the pressure in the upper tip of the dike and also, as a result of the way the dike is formed from its mantle source region, for the pressure in the dike at its lower tip.

The pressure in the upper dike tip, P_t, has commonly been assumed to be buffered by the saturation pressure of the most soluble volatile, on the grounds that, if the pressure tries to decrease below this value, more of the volatile will be exsolved, increasing the size of a pure-gas cavity in the dike tip but maintaining the pressure (Lister and Kerr, 1991; Rubin, 1993). The most soluble major volatile in the case of lunar basalts is likely to be H_2O present in amounts of up to ~1000 parts per million (Hauri et al., 2011). Newcombe et al. (2017) found the solubility of water in lunar basalts at low partial pressures of water to be approximately $2.2 \times 10^{-6} P^{0.5}$ where n_d is given as a mass fraction and the pressure P is expressed in Pascals. Over the pressure ranges of interest this is not greatly different from the solubility, n_d, of water in terrestrial mafic magmas, $n_d = 6.8 \times 10^{-8} P^{0.7}$ (Dixon, 1997). These functions imply that 1000 ppm water would saturate at a pressure in the range ~0.3 to 0.9 MPa. An alternative way of estimating the dike tip pressure was suggested by Wilson and Head (2017a), based on the principle that the CO gas which is the dominant component of the volatiles released from lunar magmas (Sato, 1976; Fogel and Rutherford, 1995) would form a foam in the uppermost part of the dike that would cease to be stable when the pressure fell below the value that caused its volume fraction to reach some critical stability level of order 85% (Jaupart and Vergniolle, 1989). This implied a dike tip pressure close to 1.0 MPa. Most recently, Rutherford et al. (2017) have re-evaluated the pattern of volatile release from the magma forming the orange picritic glass pyroclasts sampled by the Apollo 17 mission, adopting these as typical of other lunar eruptives. They find that the release of volatiles into the vapor phase in lunar magmas is complex, but a major increase of water

release occurs at a pressure close to 2 MPa, and we adopt this as the best current estimate of P_t, with the caveat that the foam stability criterion implies that the pressure would in any case not be less than ~1 MPa (see also Wilson and Head, 2017b).

The pressure in the lower tip of the dike is determined by the process of dike formation. The dike grows from a partial melt zone driven by the difference, $\Delta\rho$, between the density of the surrounding mantle source rocks, ρ_m, and the density of the liquid magma, ρ_l. Wilson and Head (2017a) show that the dike disconnects from the source zone when it has reached a length L that is a factor π times greater than the vertical extent of the source zone and that the excess pressure at the base of the dike at this time is P_e where

$$P_e = \pi^{-1} g\, \Delta\rho\, L \tag{1}$$

Therefore the absolute pressure in the dike magma at the bottom of the dike is the weight of the magma, $g\, \rho_l\, L$, plus this excess pressure, i.e., a total of $\pi^{-1}\, g\, L\, [\rho_m + (\pi - 1)\, \rho_l]$. The pressure difference between the upper and lower tips of the dike is therefore $\{\pi^{-1}\, g\, L\, [\rho_m + (\pi - 1)\, \rho_l] - P_t\}$ and dividing by the vertical length of the dike, L, the average value of the total pressure gradient, P_t', in the magma column is

$$P_t' = \pi^{-1}\, g\, [\rho_m + (\pi - 1)\, \rho_l] - \left(\frac{P_t}{L}\right) \tag{2}$$

Similarly the average value of the pressure gradient driving the magma flow, P_f', is

$$P_f' = \pi^{-1}\, g\, [\rho_m - \rho_l] - \left(\frac{P_t}{L}\right) \tag{3}$$

If P_t were zero, both of these pressure gradients would be independent of the dike length L. Since P_t is not zero, we need values for the likely range of dike sizes leaving the mantle, which can be obtained from Wilson and Head (2017a, their Table 2). Table 1 shows the range of vertical dike lengths, L, that correspond to dikes capable of feeding intrusions in FFCs on the lunar nearside, together with the total volumes, V, of magma in these dikes. These examples range from dikes that just penetrate to within a few km of the surface, through dikes that would have produced eruptions on the nearside, to dikes that would have almost, but not quite, reached the surface on the farside. The selection therefore covers the entire range of dikes that could possibly be linked to nearside FFC formation. Each example in Table 1 also shows the average values of the total pressure gradient in the dike and the part of the pressure gradient driving magma flow. The values are based on a magma density of 2900 kg m^{-3}, at the lower end of the range suggested by Kiefer et al. (2012), and a mantle density of 3260 kg m^{-3}, from Wieczorek et al. (2013). The total gradients span the range 4841.2 to 4862.4 Pa m^{-1}, a variation of only ~0.4%; clearly the size of the term (P_t / L) in equation (2) is so much smaller than the density terms that its influence is negligible. The pressure gradients driving magma flow have a stronger dependence on (P_t / L): the range, 143.20 to 164.4 Pa m^{-1}, represents a 14% variation.

Using the pressure in the dike tip and the pressure gradient in the dike, the absolute pressure in the dike can be found as a function of depth below the surface. This serves two purposes. First, the magma pressure at each depth can be compared with the lithostatic pressure in the crust at the same depth. The difference between these, P_d, will be a measure of the initial excess pressure available to prop the sill open and drive magma into it. This pressure must be at least equal to the weight of the overlying crust for sill formation to occur. Second, the bulk density of the magma can be found as a function of depth for any given assumed volatile content and hence the level where the magma is neutrally buoyant can be located, since this may also be a factor influencing where sill injection occurs. There is, however, a complicating factor. The pressure gradient driving magma motion through a dike may be significantly non-uniform. As magma enters the narrower part of the dike towards its upper tip, a greater pressure gradient is needed to drive the same flux through a narrower gap at higher speed. This process has been treated for dikes propagating from large-volume magma sources where the source pressure is essentially constant, and a very large pressure gradient may be present just below the dike tip - see Rubin (1995, his Fig. 6b). However, the case of magma flow in isolated dikes that have pinched off from their source has not been treated in the same detail, and differs in that the magma must recirculate as the dike rises. Magma must flow upward in the center of the dike at a speed approximately twice as large as the rise speed of the dike as a whole, then move away from the center-line near the top, slowly upward near the wall and finally back in toward the center-line near the base (Head et al., 2002). We treat two cases. In the first the total pressure gradient is assumed to be constant at all depths, and in the second the part of the gradient driving magma flow is weighted by the reciprocal of the dike width as the upper dike tip is approached to make a first-order allowance for the increased gradient (Rubin, 1995) as magma moves into the narrow part of the dike.

Figure 3 shows the magma pressure and the lithostatic pressure in the crust as a function of depth below the surface for the constant-gradient case when the upper tip of the rising dike is 1 km beneath the surface. The magma pressure is based on the above 2 MPa tip pressure and a constant total pressure gradient of 4851.8 Pa m^{-1}, the average of the above 4841.2 to 4862.4 Pa m^{-1} range. The lithostatic load of the crust is found by integrating the density multiplied by the acceleration due to gravity, assuming that the density has the average value of ρ_c = ~2550 kg m^{-3} as found by Wieczorek et al. (2013) but increases linearly from 2450 kg m^{-3} at the surface to 2650 kg m^{-3} at the base of the crust at 30 km to allow for some compaction with depth. Figure 3 shows that at depths below the surface smaller than ~3.3 km the internal magma pressure is less than the external stress, but at all greater depths the internal pressure is greater than the load of the overlying crust and sill injection is possible. The exact depth at which a sill might form would depend on the tensile strength of sub-crater breccia, likely to be at least a few MPa for breccias (Roy et al., 1981). For dikes that penetrate even closer to the surface, sill injection is possible at shallower depths. Figure 4 shows how the minimum sill injection depth varies with the depth of the dike top. Provided the dike top penetrates within ~2 km of the surface, sill formation could occur over depths down to ~9 km. Next, the effects of assigning a greater pressure gradient near the dike top are explored in Figures 5 and 6. Figure 5 has a similar trend to Figure 3 but with some non-linearity for shallow dike tops. The effect of the varying pressure gradient is to make sill injection possible at a shallower depth for a given depth of dike top. This result is underlined by Figure 6, which is the equivalent of Figure 4 for the constant-gradient case. Whereas in Figure 4 a dike would have had to penetrate to within ~1 km of the surface to cause a sill injection at a depth of 3 km, in Figure 6 sill injection at the 3 km depth would only

require the dike top to reach within ~2.2 km of the surface. The constant-gradient examples represent the lower bound on magma driving pressure and the upper bound on intrusion depth. We expect reality to lie closer to the variable pressure gradient cases shown in Figures 5 and 6. This implies that for intrusions at depths of ~5 km beneath the floors of the larger FFCs, excess magma pressures driving sill injection of at least 5 MPa are likely, with higher pressures for deeper sills. These pressures are comparable to, but typically slightly less than, those found by Jozwiak et al. (2012) when modelling the elastic stresses controlling intrusion formation. They are also within the range of driving pressures assumed by Thorey and Michaut (2014) in their treatment of the dynamics of lateral growth of intrusions, though no specific values are given in that paper.

Figures 4 and 6 have additional implications. As plotted, they imply a minimum depth for a sill intrusion for any given depth of the dike top below the surface. However, they can also be regarded as implying the maximum depth of the dike top that allows an intrusion to occur at a given depth. A plausible assumption made by many authors is that FFC intrusions occur near or just above the base of the breccia lens beneath the crater floor. Orphal (1979) summarizes data for impact and explosion craters up to ~10 km in diameter suggesting that the depth from the surface to the base of the brecciated zone is 32% of the crater diameter. Data are also given for the thickness of the breccia zone and an empirical fit to the data implies that the breccia thickness increases in proportion to the crater diameter to the power 1.318, thus becoming disproportionally large for large craters. We consider it unsafe to extrapolate Orphal's thickness (1979) data to the largest FFCs, but if we accept the data for the depth to the base of the breccia, and use the relationship between fresh crater depth and diameter given by Jozwiak et al. (2012, their Fig. 13), we can find the distance of the base of the breccia lens beneath the fresh crater floor and, assuming that the intrusion takes place there, infer the maximum depth of the dike top that would allow this to occur. Figure 7 shows the result; the two curves in the figure represent the effects of the two assumptions about the pressure gradient in the magma, and again reality probably lies closer to the solid line for the variable pressure gradient than the broken line for the constant gradient. Not unexpectedly, there is much less chance in large craters than in small ones of the top of a dike that eventually feeds a sill at the base of the breccia lens approaching close enough to the crater floor to produce some kind of visible modification or minor eruption.

The alternative assumption about the location of sills is that they form at the base of an impact melt sheet. Data in Cintala and Grieve (1998, their Figure 17) give the average thickness of the melt sheet expected in lunar craters as a function of the crater diameter, shown in Figure 8. Combined with the information shown in Figures 4 and 6, these melt sheet thicknesses imply that even in the largest FFCs, with diameters approaching 200 km, dike tops would have to approach within 300 m of the surface to allow intrusions at the base of the melt sheet, with even shallower tops for smaller craters. This almost certainly implies that eruptions onto the floor of the crater would occur in these cases, in which case it is not clear why a sill would also be intruded. This suggests that sill intrusions immediately beneath impact melt sheets are rare.

Finally we consider the implications of the magma density. Rutherford et al. (2017) made a detailed investigation of the amount and composition of likely lunar magma volatiles released over various pressure ranges based on analyses of the orange picritic glass pyroclasts sampled by the Apollo 17 mission. By assuming that the release pattern of each significant volatile species varies linearly with pressure, the mass fractions of CO, H_2O, SO_2, H_2S, COS and F present in the vapor phase as a function of pressure shown in Figure 9 are found. If these

mass fractions are denoted n_{CO}, n_{H2O}, n_{SO2}, n_{H2S}, n_{COS} and n_F, respectively, the bulk density, β, of the magma is given as a function of the pressure, P, by

$$\beta^{-1} = \left(\frac{Q\,T}{P}\right) \sum_{j=1}^{j=6} \left(\frac{n_j}{m_j}\right) + \left(\frac{1 - n_t}{\rho_l}\right) \quad (4)$$

where the subscript j takes the values CO, H2O, SO2, H2S, COS and F, and $n_t = \Sigma(n_j)$ is the total gas mass fraction present. The perfect gas law has been used as an adequate approximation and Q and T are the universal gas constant, 8314 J kmol^{-1} K^{-1}, and the magma temperature, say 1500 K, respectively. Figure 10 shows the variation of crust and magma densities with depth below the surface when the pressure gradient in the dike is assumed to be constant. The dike top is assumed to be 1 km below the surface and curves are shown for the nominal total mass fraction of gas released, 3400 ppm, and for hypothetical more volatile-poor magmas releasing 2000 and 1000 ppm total gas. Neutral buoyancy occurs where each magma curve crosses the crust curve, at a depth ranging from ~3 km below the dike top for the nominal 3400 ppm total volatile contents to ~1.3 km for 1000 ppm total volatiles. The equivalent calculations using the variable pressure gradient are shown in Figure 11. Neutral buoyancy depths are in this case much shallower, ranging from ~1.7 km for 3400 ppm gas to ~1 km for 1000 ppm. In general, the depths of neutral magma buoyancy are less than the likely depths of intrusions based on the pressure values, supporting the conclusion of Maccaferri et al. (2011) that neutral buoyancy alone is not the controlling factor in determining sill injection.

Once sill injection begins, magma flow conditions change because the magma column has an ever decreasing vertical extent as the sill grows in horizontal length, and an increasing proportion of the pressure gradient in the magma is in the magma flowing horizontally into the sill. Models of the detailed dynamics of sill injection need to take account of the changing pressure at the point where the feeder dike joins the sill and of the continuity of magma mass flux between the dike and the sill. Thorey and Michaut (2014) incorporated some of these factors into a model by Michaut (2011) and enhanced the model to take account of the topography of the crater hosting the intrusion. They demonstrate that their model can explain many of the morphological features of FFCs, but base it on somewhat different assumptions from those used here. Thus, they assume that the origin of the pressure at the point where magma is injected into the sill is the removal of crustal material at the time of crater formation, whereas we relate it to the arrival of a dike from the deep mantle (Wilson and Head, 2017a) at a time and place entirely unrelated to the formation of the crater. Nevertheless, both treatments assume comparable depths of magma origin. Next, they (Michaut, 2011; Thorey and Michaut, 2014) assume that the sill is fed by a circular conduit with radius up to ~100 m, whereas we (Wilson and Head, 2017a) assume that it is fed by a planar dike that has a horizontal thickness of order 100 m but a horizontal length that could easily be tens of km, leading to potentially different relationships between magma volume flux and conduit geometry. But again, many of the implied magma volume fluxes overlap between the two models. Finally, Thorey and Michaut (2014) assume that the response of the rocks above the sill is elastic, at least until fractures occur in the surface layers at the edge of the crater floor, whereas we infer that at least part of the response of the breccia material may be plastic. This suggests that laccoliths or bysmaliths, which have a greater thickness to width ratio than sills, might form preferentially in

FFCs if the intrusion does not reach the margin of the breccia lens, or if surface fracturing occurs at locations other than the crater edge. Nevertheless, the range of intrusion thicknesses implied by Thorey and Michaut's (2014) model overlaps with that inferred from gravity data by Jozwiak et al. (2012). We therefore do not explore issues related to the intrusion dynamics further. Instead, we evaluate the expected relationships between the volumes of feeder dikes and the intrusions that they produce by considering the conditions in the intruded magma and its feeder dike after emplacement is completed so that all stresses have been relaxed.

B. Phase 2 - sill emplacement

Figure 12 shows the various length scales involved after the completion of the intrusion of a sill beneath the floor of an impact crater. All pressure gradients due to magma motion have become zero and only static pressures are present. The intrusion has been injected at a depth Y below the original lunar surface into the breccia of a crater of radius R and depth D, and has grown to a thickness S. The average density of the crust is ρ_c as before, and the density of the mantle is ρ_m. The bulk density of the vesicular liquid magma is ρ_{lc} in the part of the dike within the crust and ρ_{lm} in the part of the dike within the mantle, differing values being used to allow for the effects of differing amounts of volatiles being released as a function of the varying pressure and hence depth. Let the pressure at the base of the crust be P_c. Under the central parts of a large crater, such that $R >> C$, the crustal thickness is effectively (C - D) and so

$$P_c = \rho_c \, g \, (C - D) \tag{5a}$$

However, under a sufficiently small crater, where $R << C$, the influence of the presence of the crater on the stress due to the bulk of the crust is small, and a good approximation is

$$P_c = \rho_c \, g \, C \tag{5b}$$

In practice, with C of order 30 km on most of the lunar nearside and ~50 km on most of the farside, we may take "large crater" to mean R > ~50 km and "small" to mean R < ~10 km.

The pressure in excess of the local lithostatic load in the magma where the dike crosses the crust-mantle boundary is P_e where

$$P_e = (\rho_m - \rho_{lm}) \, g \, Z \tag{6},$$

and so the absolute pressure in the magma at this point is P_b where

$$P_b = P_e + P_c \tag{7}.$$

The pressure in the magma at the level of the top of the sill is P_s, and its value is P_b minus the weight of the magma in the column of length ($X + S$), where

$$X = (C - Y) \tag{8},$$

so that

$$P_s = P_b - \rho_{lc}\, g\, (C - Y + S) \tag{9}.$$

The lithostatic pressure in the crustal rocks at the depth of the top of the sill is P_L, where for a large crater

$$P_L = \rho_c\, g\, (Y - D - S) \tag{10a},$$

and for a small crater

$$P_L = \rho_c\, g\, (Y - S) \tag{10b}.$$

We postulate that the sill stops growing, laterally and vertically, when the internal magma pressure P_s is equal to the external pressure P_L, i.e., the sill intrusion just supports the weight of the overlying crust. We then have, combining the above equations,

$$(\rho_m - \rho_{lm})\, g\, Z + \rho_c\, g\, (C - D) - \rho_{lc}\, g\, (C - Y + S) = \rho_c\, g\, (Y - D - S) \tag{11a}$$

for a large crater and

$$(\rho_m - \rho_{lm})\, g\, Z + \rho_c\, g\, C - \rho_{lc}\, g\, (C - Y + S) = \rho_c\, g\, (Y - S) \tag{11b}$$

for a small crater. Simplifying these expressions, we find that for both large and small craters,

$$Z = \frac{(\rho_{lc} - \rho_c)}{(\rho_m - \rho_{lm})}(C - Y + S) \tag{12}.$$

Although this is independent of the crater depth D, note that (Y - S) cannot be less than D: the sill must lie beneath the crater floor. Combining equations (8) and (12) shows that, in its final configuration, the ratio of the vertical extents of the dike below and above the crust-mantle boundary, (Z / X), is given by

$$\frac{Z}{X} = \frac{(\rho_{lc} - \rho_c)}{(\rho_m - \rho_{lm})}\left(1 + \frac{S}{C - Y}\right) \tag{13}$$

Jozwiak et al. (2012) infer that sill thicknesses, S, range from ~140 m to ~2 km, and that for the largest FFC craters the intrusion depths, Y, might be as much as ~7 km for craters in the C = 30 km thick nearside crust, so that [S / (C - Y)] will be of order 0.05 to 0.1. The values adopted for ρ_c and ρ_m are 2550 and 3260 kg m^{-3}, respectively, from Wieczorek et al. (2013). If we use the vesicle-free magma density of ρ_l = 2900 kg m^{-3}, as before, we find (Z / X) = 0.97, implying a dike that is nearly symmetrical about the crust-mantle boundary. However, because the vesicular magma densities ρ_{lc} and ρ_{lm} will both be somewhat less than ρ_l, this result is only approximate, but serves to show that Z and X will be similar. Note also that this result is very sensitive to the value adopted for ρ_l. If a value near the upper end of the lunar basalt density range of Kiefer et al. (2012) is used, say ρ_l = 3150 kg m^{-3}, and no change is made to the value assumed for the density of the mantle, (Z / X) becomes 5.45, and the dike must extend much further into the mantle. We do not pursue this option further because, as we show below, this would pose serious problems for the existence of extensive shallow sills.

The pressure holding the dike open is the excess pressure in the magma where the dike crosses the crust-mantle boundary, i.e. P_e. The mean width of the dike in its final configuration is W where

$$W = \left(\frac{1-\upsilon}{\mu}\right)\left[\left(\frac{\pi}{2}\right) P_e \, (Z\,X)^{1/2} - 0.33\, g\, [X^2(\rho_{lc} - \rho_c) - Z^2(\rho_m - \rho_{lm})]\right] \quad (14)$$

Here ν and μ are the Poisson's ratio and shear modulus for the host rocks, taken as 0.25 and 4 GPa, respectively (Bieniawski, 1984; Rubin, 1990), and the treatment of Rubin and Pollard (1987) was slightly modified by Wilson and Head (2017a) to take account of the dike asymmetry. Assuming that the final shape of the dike after it has finished causing the injection of the sill is such that it has about the same horizontal extent as its vertical extent, i.e. a "penny" shape, the volume, V, of magma remaining in the dike can be approximated by

$$V = \pi\, X\, Z\, W \quad (15)$$

At this point we introduce the effects of the presence of the volatiles in the magma in order to evaluate ρ_{lc} and ρ_{lm}. The bulk density of the magma is given as a function of the pressure by equation (4), but we require it as a function of depth throughout the dike that has fed the sill. The procedure is as follows. First, the depth Y of the base of the sill and the thickness S of the sill are selected and a first approximation to Z is found using equation (13) with ρ_l substituted for ρ_{lc} and ρ_{lm}. Our basic assumption is that the pressure at the top of the sill is equal to the overlying load of the crust, which we have specified earlier as increasing linearly from 2450 kg m^{-3} at the surface to 2550 kg m^{-3} at the crust-mantle interface, so selecting Y and S also fixes the pressure in the magma column in contact with the top of the sill. Equation (4) is next used to find the bulk magma density, β, at this pressure. The fact that the pressure gradient dP/dz is equal to ($\beta\, g$) is then used in a spreadsheet program to track by numerical integration the change of density and pressure with depth, past the base of the crust and as far as the base of the dike. The average values of the bulk density in the upper and lower parts of the dike are thus found and used in equation (13) to produce an improved value of Z, and the process is repeated until

adequate convergence is reached. Equations (14) and (15) are then used to find the mean width of the residual dike and the volume of magma remaining in it.

Note that this treatment tacitly assumes that the released gases are distributed uniformly throughout the magma during the dike and sill emplacement. This is justified by noting that gas bubbles forming in magmas nucleate with radii of order 10 μm (Sparks, 1978). The typical absolute pressures in the sill-feeding dikes are found from the above spreadsheet to be in the range 12 to 280 MPa. In decompressing from 280 MPa to 12 MPa a bubble with radius r = 10 μm would expand to a radius of $[(280/12)^{1/3} \times 10 =]$ ~29 μm. Balancing the buoyancy $[(4/3)\ \pi\ r^3\ (\rho_l - \sigma)\ g]$ against the viscous drag $[6\ \pi\ \eta\ r\ u]$, the rise speed, u, of a gas bubble of density σ in magma of density ρ_l and viscosity η is

$$u = \frac{2\ r^2\ (\rho_l - \sigma)\ g}{9\ \eta} \qquad (16)$$

Typical gas densities in the 12 to 280 MPa pressure range are 30-670 kg m^{-3}, so $(\rho_l - \sigma)$ ranges from 2230 to 2870 kg m^{-3}. Assuming a lunar basalt magma viscosity of ~1 Pa s, values of u are at most ~ 0.3 μm s^{-1}. Typical rise speeds of the magma in dikes feeding sills are ~10 m s^{-1} (Wilson and Head, 2017a) and continuity dictates that average injection speeds into the sills will be of the same order. With horizontal injection distances of up to 100 km, total emplacement times are of order 10^4 s (~3 hours), and with vertical rise distances of ~500 km gas bubbles would drift upward relative to the magma around them during this time by no more than ~3 mm. Changing the assumed magma viscosity by an order of magnitude would change the bubble rise speed by the same factor, but this would not change the conclusion that the gas bubbles are effectively frozen into the magma during the entire sill formation event.

The results of the above considerations are summarized in Tables 2 and 3 for sills beneath FFCs on the nearside and farside, respectively, of the Moon. Each table is calculated for a sill intruded at a depth of Y = 5 km below the lunar surface, thus placing it around the base of the breccia lens for small craters, within the breccia lens for larger craters, and at the top of the breccia lens for the largest FFCs. With Y = 5 km the dike extends for X = 25 km above the crust-mantle boundary on the nearside and 45 km above the crust-mantle boundary in the 50-km thick farside crust. Each table has three parts, for released volatile totals of 1000, 2000 and 3400 ppm, and covers a range of sill thicknesses, S, up to 2 km. The parameters listed are the extent of the dike below the crust-mantle boundary, Z, the excess pressure in the dike at the crust-mantle boundary, P_e, the mean dike width, W, and the volume of magma remaining in the dike after sill intrusion is complete, V. Equivalent tables have been constructed for other depths of sill intrusion, and the variations of the residual dike magma volume for intrusion depths of 3, 5 and 7 km, on both the lunar nearside and farside, are shown in Figure 13 as a function of the total released magma volatile amount. Note that the residual magma volume increases as the released volatile amount decreases.

The volume of magma injected into the sill is the original volume of the dike while it was an isolated structure ascending though the lunar mantle, given in Table 1, minus the amount remaining after the sill injection, given by equation (15) and listed in Tables 2 and 3 for an intermediate depth of sill intrusion. Wilson and Head (2017a, their Table 2) gave examples of the geometries of lunar dikes leaving mantle partial melt zones. They divided these into dikes that failed to erupt anywhere on the Moon, those that erupted on the nearside but not the farside,

and those that erupted on the farside. We select from the results of Wilson and Head (2017a) all of the dikes that approach within a few km of the surface on the nearside and on the farside, since this covers the range of conditions that allow dikes to feed shallow intrusions anywhere on the Moon without causing a surface eruption. The volumes of these feeder dikes, given in Table 1, range from ~70 to ~1130 km^3. Our calculated residual dike volumes after sill injection on the nearside given in Table 2 range from 103 to 316 km^3. The equivalent residual volumes in dikes on the farside given in Table 3 range from 1540 to 3340 km^3. Comparing the volumes before and after the sills are formed leads to two important conclusions.

First, all of the farside residual volumes are greater than the volumes available from the mantle feeder dikes. This is, of course, impossible: the residual volume is by definition the amount of magma left beneath the surface after some of the magma in the feeder dike has been used to inject the sill, so the initial magma volume in the feeder dike leaving the mantle must be greater than the residual volume after the sill has been formed. The implication is that, to inject sills beneath impact craters on the farside, feeder dikes would have needed to contain a great enough volume of magma that they would have erupted that magma onto the surface if they had not been intercepted by a crater. Since surface eruptions on the lunar farside are rare, and it is unlikely that every dike approaching the surface on the farside will intersect a large crater, we would expect that only a very small fraction of the impact craters on the farside crust should have become floor-fractured craters, and this is indeed what is observed (Jozwiak et al., 2012). The paucity of farside floor-fractured craters therefore reinforces the implications of the low incidence of farside surface eruptions, which is that there was an upper limit to the volume of melt that could be extracted in any one dike-formation event from a partial melt zone in the lunar mantle. Wilson and Head (2017a) show that this restriction implies that there was an upper limit of order 30 km to the vertical extents of partial melt source zones in the mantle. We can now justify the earlier assertion that there is little value in using a larger magma density than the one used so far from the range suggested by Kiefer et al. (2012), because if we do so, the volume of magma remaining in the feeder dike after sill intrusion increases, making less available for the sill itself, and this exacerbates the problem of understanding the formation of the largest FFC intrusions.

The second implication of comparing the above volumes specifically relates to the floor-fractured craters on the lunar nearside. The magma volumes available for injection into sills range from zero (nominally ~70 - 103 = - 33 km^3, but again negative values are meaningless) to as much as (~1130 - 316 =) ~814 km^3. Floor-fractured craters have diameters from ~10 km to up to 200 km. If sill intrusions occupied 90% of the floor area of each of these crater sizes, the above 814 km^3 volume implies that their thicknesses could range up to ~12 km for the small craters, much larger than the hundreds of meters estimates of Jozwiak et al. (2017) from floor uplift and gravity data, but only up to ~30 m for the largest craters, much smaller than the Jozwiak et al. (2017) estimates of more than 1 km. Thus while many of the intrusions identified in smaller craters can readily be explained by a single intrusion event, this is not possible for the thickest examples in the largest craters. The most extreme case is that of Humboldt, which has a diameter of 207 km and an estimated sill thickness from its floor uplift of ~2 km (Jozwiak et al., 2012). The intrusion volume implied by these values is ~60,000 km^3, vastly greater than our ~814 km^3 upper limit. However, examination of the band-filtered Bouguer anomalies for this crater (Fig. 2b of Jozwiak et al., 2017) shows that the anomalies underlie only about 9% of the subsurface area, so only this fraction is likely to host intruded magma, reducing the volume estimate to ~5,300 km^3. Similarly for Alphonsus, the volume derived from the floor uplift of

900 m over 90% of the area corresponding to the 119 km diameter is 9,000 km^3, but the band-filtered Bouguer anomalies show that only 11% of the subsurface is likely to consist of intrusions, making the implied volume only ~990 km^3. The maximum feeder dike volume predicted by Wilson and Head (2017a) to be capable of producing an eruption on the nearside of the Moon is, as noted above, no more than ~1130 km^3, so that even if all of the magma in such a large dike were transferred into the sill, instead of part of it remaining in the crust as expected and implied by Table 1, it is clear that, although a single intrusion event could just explain Alphonsus, it would fail by a factor of nearly 5 to explain Humboldt. The implication is that the largest FFC intrusion volumes must represent the results of some small number of separate dikes intersecting the sub-surface of the largest craters in separate events. Once one sill has been emplaced at the base of, or within, the breccia zone beneath the crater, it is likely that subsequent dikes approaching from below may intrude along the density boundary that the earlier event put in place. Alternatively, the second and any subsequent intrusions may be unconnected with the earlier ones, a suggestion supported by the dispersed spatial arrangements of the patches of erupted material and the heterogeneity of the gravity signal in Humboldt.

The above magma volume comparisons are drawn on the basis of sill intrusions at $Y = 5$ km depth below the lunar surface, and therefore at varying depths below the floors of FFCs, but the trends in Figure 13 show that the residual dike magma volumes depend only weakly on Y. Also, the full spread of likely lunar magma volatile contents has been used in making the comparisons, and so the above conclusions should be robust.

C. Post-emplacement sill evolution

The timescale for sill generation has been shown above to be only a few hours, during which time gas bubble migration in lunar magmas is small. However, the time scale for the cooling and solidification of a sill will be much longer, and bubble migration may be significant while this is taking place. A reasonable estimate of the cooling time can be found from the treatment of cooling lava lakes given by Turcotte and Schubert (2002) in which the thickness, B, of the solid boundary layer as a function of time, t, is given by

$$B = 2\,\lambda\,(\kappa\,t)^{1/2} \tag{17}$$

Here κ is the thermal diffusivity of rock, ~10^{-6} m^2 s^{-1}, and λ is a constant given by the solution of

$$\frac{\pi^{1/2}\,L}{c\,\Delta T} = \frac{e^{-\lambda^2}}{\lambda\,\mathrm{erf}(\lambda)} \tag{18}$$

where L is the latent heat of solidification of magma, ~400 kJ kg^{-1}, c is the magma specific heat, ~1 kJ kg^{-1}, and ΔT is the temperature difference between the magma temperature and the ambient environment, ~1000 K for a magma temperature of 1500 K and an ambient temperature at 5 km depth of ~450 K (Manga and Arkani-Hamed, 1991). Using these values λ is ~ 1.2 and so to solidify ~20% of the thickness of a 100 m thick sill (10% at the top and 10% at the base) requires ~21 days (Figure 14a), during which time gas bubbles will migrate ~0.5 m. However, to solidify ~20% of the thickness of a 1 km thick sill requires ~58 years, and gas bubbles could migrate a little over 500 m in this time, ensuing that nearly all of the gas in a sill of this thickness could

first form a foam layer (Figure 14b) and then, as the foam collapsed due to downward liquid percolation between gas bubbles, a gas layer under a chilled magma layer adhering to the roof of the sill. Upward gas bubble migration will be shown below to produce an increase of the sill thickness. However, subsequent solidification and cooling of the liquid magma produce volume changes that also cause the vertical extent of the intrusion to change, in this case to a smaller value (Figure 14b). We note that the formation of a free gas layer at the top of the sill could provide the potential for gas to escape into the overlying crust if the chilled magma in contact with the overlying crustal rocks developed fractures. However, by definition there must always be a layer of partially cooled but still plastic magma between the uncooled magma in the core of the sill and the brittle solid magma at the contact between the sill and the country rocks, and this plastic magma would be forced into cracks, thus sealing them. We therefore think that gas loss during the uplift phase would be minimal unless a major fracture formed that penetrated all the way from the surface into the sill. If that happened, of course, an eruption onto the floor of the crater would occur.

To investigate the consequences of these processes we start with the variations of magma pressure with depth in dikes feeding sills described in the previous section. Immediately after its emplacement, the pressure variation with depth in a sill is the same as that in the part of the dike in contact with the sill because, as was just demonstrated, the amount of movement of gas bubbles during this period was negligible. It is convenient to derive analytical expressions for the variations with depth of the pressure and volume fractions of gas and magmatic liquid. These can be found using equation (4) together with the definition that the rate of change of pressure with vertical position is equal to the bulk density of the magma multiplied by the acceleration due to gravity, i.e.

$$\frac{dP}{dh} = \beta\ g \tag{19}$$

Substituting the expression for β from equation (4) and integrating allows the pressure, P, to be found as a function of the depth H below the top of the sill where the pressure is P_0:

$$g\ H = Q\ T \sum_{j\,=\,1}^{j\,=\,6} \left(\frac{n_\mathrm{j}}{m_\mathrm{j}}\right) ln\left(\frac{P}{P_0}\right) + \left(\frac{1 - n_\mathrm{t}}{\rho_\mathrm{l}}\right)(P - P_0) \tag{20}$$

Furthermore, the first and second terms on the right-hand side of equation (4) are the partial volumes of gas and liquid, respectively, in the magma, and so the total vertical extent of the region occupied by gas, E_g, between the pressure levels P_0 and P is

$$E_\mathrm{g} = \left(\frac{Q\ T}{g}\right) \sum_{j\,=\,1}^{j\,=\,6} \left(\frac{n_\mathrm{j}}{m_\mathrm{j}}\right) ln\left(\frac{P}{P_0}\right) \tag{21}$$

and similarly the vertical extent of the region occupied by liquid, E_l, between the pressure levels P_0 and P is

$$E_l = \left(\frac{1 - n_t}{g\ \rho_l}\right)(P - P_0) \tag{22}$$

where, of course, H is equal to $(E_g + E_l)$.

These vertical variations of pressure and gas and liquid volume fractions are used as the starting point for finding the effects of migrating gas bubbles. The pressure acting on each gas bubble decreases as it rises, and the bubble expands. When all of the gas has migrated through the foam stage to the final state, i.e., a layer of gas above a bubble-free liquid, the pressure in the gas must still be great enough to support the weight of the overlying crust, i.e. must be equal to P_0. Strictly speaking there is a vertical pressure gradient in the gas, but the scale heights on the Moon at a magmatic temperature of 1500 K, given by $[(Q\ T) / (m_j\ g)]$, for CO, H_2O and SO_2, the dominant species and the species with the lowest and highest molecular masses, respectively, are ~275, 428 and 120 km, respectively, so the pressure change in pockets of gas hundreds of meters in vertical extent is negligible. The consequence of the gas migration is therefore the uplift of the roof of the intrusion (Figures 2b, 14b). The amount of uplift is found as follows. The gas mass per unit horizontal area of the sill down to any given pressure level is by definition equal to a fraction n of the liquid mass down to that level, given by E_l from equation (22) multiplied by the liquid density ρ_l. The density of each volatile species, now all present in the layer with pressure P_0, is given by the gas law as $[(m_j\ P_0) / (Q\ T)]$. Therefore the new gas volume per unit horizontal area of the sill is the mass per unit area divided by the new density, and the uplift, U, is the difference between the old and new gas volumes per unit area. Combining all of the above steps we find

$$U = \left(\frac{Q\ T}{g}\right) \sum_{j\ =\ 1}^{j\ =\ 6} \left(\frac{n_j}{m_j}\right) \left[(1 - n_t)\left(\frac{P}{P_0} - 1\right) - ln\left(\frac{P}{P_0}\right)\right] \tag{23}$$

Figure 15 shows how the uplift, U, varies with sill thickness, S, for intrusions formed at 3, 5 and 7 km below the lunar surface, in each case for n_t = 1000, 2000 and 3400 ppm. The extreme case shown is a 2 km thick sill intruded at 3 km depth containing a total content of 3400 ppm volatiles, in which case the uplift would be ~30 m. The vertical extent occupied by the liquid and gas in the sill at the end of this phase is $S' = S + U$.

We now address the factors finally decreasing the sill thickness (Figure 14b). As magma cools, its density increases. The volume coefficient of thermal expansion of liquid magma is ~5 × 10^{-5}, so in cooling from an initial temperature of, say, 1500 K to a solidus of 1250 K, the volume change is 1.25%. It seems likely that as the magma cools and crystallizes the horizontal area of the sill stays constant and the liquid component is redistributed so that the thickness decreases vertically by 1.25%, i.e. a factor ~0.985. As the magma solidifies, its density increases from 2900 to ~3200 kg m^{-3}, so while any liquid remains deformation continues and the sill shrinks vertically by the additional factor [(2900/3200) =] ~0.91. Further magma shrinkage with associated roof subsidence occurs as the magma cools to the ambient temperature, ~300 K at a

few km depth in the Moon ~3 Ga ago. The volume coefficient of thermal expansion for solid magma is ~3×10^{-5}, but since it no longer has a liquid component the magma shrinks in all three spatial directions. The linear expansion coefficient is ~1×10^{-5}, so for a 950 K cooling from 1250 K to ~300 K the vertical change is a further 0.95%, a factor of ~0.99. All of these three vertical subsidence contributions act on the non-gas part of the magma that initially had a vertical extent E_l, so this changes by a factor ($0.985 \times 0.91 \times 0.99$) to ~$0.887\ E_l$. However, while the liquid and later solid magma is cooling, the gas is also cooling, from ~1500 K to ~300 K. This means that, in order to maintain the pressure P_0 needed to support the overlying crust, the gas volume must decrease by a factor [(300/1500)] = 0.2. The gas always fills the entire available space laterally, and so the vertical extent of the gas pocket before cooling, ($E_g + U$), becomes 0.2 ($E_g + U$). The final total vertical extent of the sill is therefore $S'' = [0.887\ E_l + 0.2\ (E_g + U)]$. On inserting the relevant numerical values for sills initially up to S = 2 km thick and for total volatiles contents up to 3400 ppm we find that, because the uplift amounts, U, due to gas migration are a relatively small fraction of S, the final sill thickness S'' is only very slightly dependent on the presence of the volatiles and is very close to 84% of S. Thus an initially 2 km thick sill would have a final thickness of 1.68 km (Figure 14b). Using the same extreme case illustrated above, this 2 km thick sill would have been intruded over the course of a few hours at 3 km depth by magma with 3400 ppm volatiles; the crust above it would then have been uplifted, after the initial intrusion took place, by ~30 m due to upward gas bubble migration over a period of several decades, and would then have subsided due to cooling over the course of the next several centuries by 350 meters to reach a level 320 meters below its maximum uplift (Figure 14b).

D. Predicted eruption styles associated with dike and sill injection, growth, volatile evolution and cooling

The several stages of dike and sill injection, growth, volatile evolution and cooling (Figure 14) lead to predictions concerning the eruptions styles that might accompany the different stages, and we outline these below and in Figure 16.

1) *Dike tip emplacement*: First, the initial dike emplacement event that precedes sill formation will be characterized by the arrival of the dike tip in the breccia lens below the solidified melt sheet in the FFC. The dike tip will be dominated by volatile species associated with the low pressure zone in the dike tip as it propagates toward the surface (Wilson and Head, 2003). As the dike comes to rest, there is a possibility that the pressure rise in this gas might propagate a crack to the surface and erupt small volumes of gas, pyroclastics, regolith clasts and small fragments of breccia (Figure 16a).

2) *Sill intrusion and floor uplift*: In this stage, the pressure in the dike forces magma laterally into an expanding sill (Figure 16b) that grows until the base of the crater wall is reached, where the overburden pressure of the crater rim (wall, uplift and ejecta) retards further lateral magma propagation (Figure 16c). Crater floor uplift continues, with the formation of either a tabular sill-like body or a thicker laccolith or bysmalith. Typically, the majority of the deformation takes place at the outer margin of the sill as the sill stops growing laterally and inflates vertically. In this environment, subsidiary dike emplacement can take place along the uplift margin (Figure 16c). In this case, several eruptive styles may occur: a) the subsidiary dike reaches the surface, causing effusion of lava out onto the crater floor; such extrusions are often located along graben that form at the edge of the crater floor (Head and Wilson, 2017), and flood the graben, as in the case of Humboldt (Figure 1b). b) If the subsidiary dike nears, but does not

breach the surface, then the upper part of the dike can accumulate volatiles under a chilled dike tip, and build up pressure until an explosive eruption occurs; such a vulcanian eruption would incorporate wall rock and produce a dark halo crater composed of fragmented solidified basalt cap, wall rock, and any disaggregated glassy foam (Head and Wilson, 1979). c) If the subsidiary dike reaches close enough to the surface such that near-surface extensional stresses form a graben (Head and Wilson, 1979), but is too deep to erupt to the surface, the top of the dike may degas as it cools, venting gas to the surface and causing pit craters (active) or drainage craters (passive) along and within the graben. Guidance to which of these several options might occur comes from consideration of the emplacement dynamics (Figure 16c); because the dike tip did not initially reach the surface, hydrostatic relations would favor intrusion along the ring fractures at this point, rather than eruption, thus favoring options b) and c).

3) *Central uplift patterns of the crater floor*: Deformation of the brittle solidified impact melt cap on the crater floor may accompany the phase of floor upbowing and uplift (Figure 16b), and some of the concentric and radial fractures seen in FFCs (Figure 1) may occur at this time (Jozwiak et al., 2017). In this case, the fracturing is expected to occur prior to the time of the rise and coalescence of nucleated gas bubbles into a foam layer and their subsequent collapse (Figure 16d), to form a gas pocket at the top of the sill. In this context, foam or gas has yet to coalesce at the top of the sill, and thus is not expected to erupt; any magma erupted to the surface, if it occurred, should be largely effusive, but the same hydrostatic arguments favor intrusion over extrusion.

4) *Subsequent gas bubble rise, foam collapse, and venting*: Following sill emplacement and floor uplift, and prior to cooling and solidification, gas bubbles will grow as they rise to the top of the sill to create a foam layer (Figure 16d). Eventually the foam layer will partially collapse due to drainage of interstitial bubble wall melt, creating an overlying gas layer. The net increase in volume that occurs during this phase will cause further stresses at the top of the sill, perhaps initiating additional fractures in the crater floor. If such fractures form during creation of the foam layer, then venting of the foam may occur, creating local pyroclastic eruptions along the fractures; alternatively, after the collapse of the foam, the eruptions may represent venting of pure gas and may form surface collapse craters along fractures rather than eruptive surface deposits. Foam and gas could also vent along the fractures that previously formed during stage 2 (sill intrusion and floor uplift). Such additional over-pressurization could also force gas-rich magma out of the marginal ring fractures to form effusive flows and local pyroclastic eruptions.

5) *Cooling and subsidence*: Finally, long-term sill cooling (Figure 14b) and associated subsidence in the ~350 m range (Figure 16e) may initiate fractures in the overlying solidified melt sheet; at this point the bubble walls of part of the foam should have drained to produce the gas pocket, the remaining foam should have solidified, and thus any venting in this late stage subsidence should be minor and consist of residual gas from the collapsed foam gas pocket.

Detailed analysis of the stratigraphy and sequence of events of floor fracturing, faulting and associated explosive and effusive eruptions of individual FFCs (Jozwiak et al., 2017) should lead to the identification of the specific eruption types accompanying these different stages of FFC history, and permit the further testing and refinement of this model.

III. Conclusions

1. Floor-fractured craters represent a class of lunar features whose characteristics are consistent with dike intrusion followed by shallow sill formation, resulting in floor uplift, degassing, intrusion cooling and solidification, and associated deformation.

2. New treatments of the generation, ascent and eruption of magma, and new understanding of melt density, and crustal thickness, density and porosity, lead to the interpretation that dikes form at the top of rising diapirs at great depth, and pinch off and rise buoyantly as disconnected bodies to the surface, reaching a neutral buoyancy level represented by the crust-mantle boundary. If the volume and vertical extent of the dike are sufficiently large, the dike will penetrate to the surface and form an eruption. Eruptions are favored in areas of thinner crust.

3. Floor-Fractured Craters (FFCs) result when dikes are capable of intruding close to the surface, but fail to erupt because of the substructure of their host impact craters, and instead intrude a sill.

4. Terrestrial field observations support the interpretation that sill initiation and injection is primarily a result of encountering a contrast in host rock lithology, rigidity, or rheology (for example, a change from brittle to ductile response), with neutral buoyancy and ambient tectonic stresses potentially contributing, but generally being secondary factors.

5. On the Moon, two candidates for this transition in FFCs are: a) the base of the solidified melt sheet, and b) the deeper boundary between the relatively less fractured crustal rocks and the base of a highly fractured, ductile breccia lens.

6. Observations suggest that if sill intrusion were controlled by the physical properties at the base of the melt sheet, dikes would be required to approach to within ~300 m of the surface, and thus eruptions would be very likely to occur, rather than the intrusions of sills. Dynamical considerations strongly favor the sub-crustal breccia lens as being the location of the physical property contrast that localizes the lateral intrusion.

7. Two phases are involved in the emplacement of sills: 1) a dike enters the crater substructure and encounters an increase in ductility (base of breccia lens) or rigidity (base of solidified melt sheet); magma rise velocity causes dike tip to overshoot; 2) magma undergoes subsequent horizontal flow to form the intrusion and raise the crater floor, being fed by the positively buoyant magma in the lower part of the dike.

8. Termination of sill lateral and vertical growth occurs when the internal magma pressure equals the external pressure; that is, when the sill intrusion just supports the weight of the overlying crust.

9. Volatiles form (CO) and are exsolved (H_2O and sulfur compounds) during the dike and sill emplacement process. Total emplacement times are likely to be less than ~3 hours and thus gas bubbles would rise only a few mm, and are not likely to coalesce into a foam.

10. The total volume of feeder dikes that can form shallow intrusions anywhere on the Moon without causing an eruption ranges from ~70 to 1130 km^3. Dynamical considerations lead to the conclusion that dike volumes are generally insufficient to form FFCs on the lunar farside; any dikes with sufficient volumes to form FFCs would have more likely resulted in farside eruptions, and thus farside FFCs should be rare.

11. Estimated magma volumes available for injection into sills on the lunar nearside range from very small to ~800 km^3, comparable to the volume implied by the observed floor uplift in many small FFCs, and thus consistent with these crater forming from a single dike emplacement event.

12. The thickest intrusion examples in the larger craters, such as Humboldt, imply volumes greatly in excess of that of a single dike emplacement event and imply that these FFCs involved multiple dike emplacement events. Comparisons of sill cooling times and dike

recurrence times strongly suggest that these events would be completely separate events, rather than injection of new magma into a still-cooling intrusion formed earlier.

13. Following emplacement of a sill in a few hours, the cooling time for the sill to undergo solidification is estimated to be years to decades, depending on sill thickness (Figure 14b).

14. During the cooling and solidification of the sill, upward migration of volatile bubbles can occur: bubbles can rise hundreds of meters to the top of the intrusion to create a foam layer. When the foam layer collapses due to downward percolation of the liquid between gas bubbles, a gas layer can form between the chilled upper layer and the cooling magma.

15. Upward gas migration produces an increase in sill thickness, while subsequent cooling and solidification cause thickness decreases (Figure 14b). An initial 2 km thick sill would have a final thickness of ~1.68 km.

16. The total volume evolution history for an intrusion initially 2 km thick can be summarized in the following steps (Figure 14): 1) Intrusion uplifts floor 2 km; 2) Gas formation and migration over several decades raises floor by ~30 m; 3) Cooling and solidification over the next century cause subsidence by ~350 m; 4) Final configuration places floor about 320 m below its initial level.

17. On the basis of the general thermal evolution of the Moon (general mantle cooling, growing lithospheric thickness, increasingly contractional global state of stress in the lithosphere; Solomon and Head, 1980), fewer FFCs are predicted to form as a function of time and when they do form, the volumes of injected magma will be smaller.

18. These predictions concerning typical dike emplacement, sill/laccolith/bysmalith formation and resulting deformation and magmatism (Figure 16) can be used as a basis to assess the nature and history of each of the ~170 FFCs mapped to date (Jozwiak et al., 2015) and to assess their individual histories (e.g., Jozwiak et al., 2017).

19. Differences in the mode of occurrence and abundance of FFCs on other planets, compared with the Moon, are likely to be related to differences in the generation and ascent of magma, and different boundaries where an increase in ductility or rigidity occur.

Acknowledgments: We gratefully acknowledge financial support from the NASA Solar System Exploration Research Virtual Institute (SSERVI) grant for Evolution and Environment of Exploration Destinations under cooperative agreement number NNA14AB01A at Brown University. JWH thanks the NASA Lunar Reconnaissance Orbiter (LRO) Mission, Lunar Orbiter Laser Altimeter (LOLA) Experiment Team (Grants NNX11AK29G and NNX13AO77G), and the NASA Gravity Recovery and Interior Laboratory (GRAIL) Mission Guest Scientist Program (Grant NNX12AL07G). LW thanks the Leverhulme Trust for funding through an Emeritus Fellowship.

References

Abdelmalak, M.M., Mourgues, R., Galland, O., Bureau, D., 2012. Fracture mode analysis and related surface deformation during dyke intrusion: Results from 2D experimental modelling. Earth and Planetary Science Letters 359–360, 93-105, doi:10.1016/j.epsl.2012.10.008

Besserer, J., Nimmo, F., Wieczorek, M.A., Weber, R.C., Kiefer, W.S., McGovern, P.J., Andrews-Hanna, J.C., Smith, D.E., Zuber, M.T., 2014. GRAIL gravity constraints on the vertical and lateral density structure of the lunar crust. Geophysical Research Letters 41, 5771–5777, doi:10.1002/2014GL060240

Bieniawski, Z.T., 1984. Rock Mechanics Design, in Mining and Tunneling. Balkema, Boston, 272 pp.

Bradley, J., 1965. Intrusion of major dolerite sills. Transactions of the Royal Society of New Zealand 3, 27–55.

Brennan, W. J., 1975. Modification of premare impact craters by volcanism and tectonism, Moon, 12, 449–461, doi:10.1007/BF00577934

Cathles, L. M., 1975. The Viscosity of the Earth's Mantle, 386 pp., Princeton Univ. Press, Princeton, N. J.

Cintala, M.J., Grieve, R.A.F., 1998. Scaling impact melting and crater dimensions: implications for the lunar cratering record. Meteoritics and Planetary Science, 33, 889–912.

Corry, C.E., 1988. Laccoliths: mechanics of emplacement and growth. Geological Society of America, Special Paper, vol. 220, 114 pp.

Crawford, G.D., Stevenson, D.J., 1988. Gas-driven water volcanism and the resurfacing of Europa. Icarus 73 (1), 66-79.

Daneš, Z. F., 1965. Rebound processes in large craters, in Astrogeologic Studies, Annu. Prog. Rep., A, pp. 81–100, U.S. Geol. Surv., Washington, D. C.

Dixon, J.E., 1997. Degassing of alkalic basalts. American Mineralogist 82(3-4), 368-378.

Dombard, A. J., Gillis, J., 2001. Testing the viability of topographic relaxation as a mechanism of the formation of lunar floor-fractured craters. J. Geophys. Res., 106(E11), 27,901–27,909, doi:10.1029/2000JE001388

Fogel, R., Rutherford, M., 1995. Magmatic volatiles in primitive lunar glasses, I, FTIR and EPMA analyses of Apollo 15 green and yellow glasses and revision of the volatile-assisted fire-fountain theory. Geochimica et Cosmochimica Acta 59, 201–215.

Francis, E.H., 1982. Magma and sediment: I. emplacement mechanism of late carboniferous tholeiite sills in northern Britain. Journal of the Geological Society of London 139, 1–20.

Gudmundsson, A., 2011. Deflection of dykes into sills at discontinuities and magma-chamber formation. Tectonophysics 500, 50–64, doi:10.1016/j.tecto.2009.10.015

Hall, J. L., Solomon, S.C., Head, J.W., 1981. Lunar floor-fractured craters: Evidence of viscous relaxation of crater topography. J. Geophys. Res., 86, 9537–9552, doi:10.1029/JB086iB10p09537

Hauri, E.H., Weinreich, T., Saal, A., Rutherford, M.C., Van Orman, J.A., 2011. High pre-eruptive water contents preserved in lunar melt inclusions Science 333, 213-215, doi: 10.1126/science.1204626

Head, J.W., Wilson, L., 1979. Alphonsus-type dark-halo craters: Morphology, morphometry, and eruption conditions, Proceedings of the Tenth Lunar and Planetary Science Conference, 2861-2897.

Head, J.W., Wilson, L., 1992. Lunar mare volcanism: stratigraphy, eruption conditions, and the evolution of secondary crusts. Geochimica et Cosmochimica Acta, 56, 2155-2175.

Head, J.W., Wilson, L., 1994. Lunar graben formation due to near-surface deformation accompanying dike emplacement, Planetary and Space Science, 41, 719-727.

Head, J.W., Wilson, L., 2017. Generation, ascent and eruption of magma on the Moon: new insights into source depths, magma supply, intrusions and effusive/explosive eruptions (Part 2: Observations). Icarus, 283, 176–223, doi:10.1016/j.icarus.2016.05.031

Head, J.W., Weitz, C.M., and Wilson, L., 2002. Dark ring in Southwestern Orientale Basin: Origin as a single pyroclastic eruption. *J. Geophys. Res., 107* (E1), doi: 10.1029/2000JE001438.

Jackson, M.D., Pollard, D.D., 1988. The laccolith-stock controversy: new results from the southern Henry Mountains, Utah. Geological Society of America Bulletin, 100, 117-139.

Jaupart, C., Vergniolle, S., 1989. The generation and collapse of a foam layer at the roof of a basaltic magma chamber. Journal of Fluid Mechanics, 203, 347–380.

Johnson, A. M., Pollard, D.P., 1973. Mechanics of growth of some laccolithic intrusions in the Henry Mountains, Utah. I. Field observations, Gilbert's model, physical properties and flow of magma. Tectonophysics, 18, 261–309, doi:10.1016/0040-1951(73)90050-4

Jozwiak, L.M., Head, J.W., Zuber, M.T., Smith, D.E., Neuman, G.A., 2012. Lunar floor-fractured craters: Classification, distribution, origin and implications for magmatism and shallow crustal structure. J. Geophys. Res. 117, E11005, doi: 10.1029/2012JE004134

Jozwiak, L., Head, J.W., Wilson, L., 2015. Lunar floor-fractured craters as magmatic intrusions: geometry, modes of emplacement, associated tectonic and volcanic features, and implications for gravity anomalies. Icarus 248, 424–447, doi:10.1016/j.icarus.2014.10.052

Jozwiak, L.M., Head, J.W., Neuman, G.A., Wilson, L, 2017. Observational constraints on the identification of shallow lunar magmatism: insights from floor-fractured craters. Icarus, 283, 224–231, doi:10.1016/j.icarus.2016.04.020

Kerr, A.D., Pollard, D.D., 1998. Toward more realistic formulations for the analysis of laccoliths. Journal of Structural Geology, 20(12), 1783-1793.

Kiefer, W.S., Macke, R.J., Britt, D.T., Irving, A.J., Consolmagno, G.J., 2012. The density and porosity of lunar rocks. Geophys. Res. Lett. 39, L07201, doi: 10.1029/2012GL051319

Le Corvec, N., Menand, T., Lindsay, J., 2013. Journal of Geophysical Research: Solid Earth 118, 968–984, doi:10.1002/jgrb.50142

Lister, J.R., Kerr, R.C., 1991. Fluid-mechanical models of crack-propagation and their application to magma transport in dykes. J. Geophys. Res. 96 (B6), 10,049–10,077.

Maccaferri, F. Bonafede, M, Rivalta, E., 2011. A quantitative study of the mechanisms governing dike propagation, dike arrest and sill formation. Journal of Volcanology and Geothermal Research 208, 39–50, doi:10.1016/j.jvolgeores.2011.09.001

Manga, M., Arkani-Hamed, J., 1991. Remelting mechanisms for shallow source regions of mare basalts. Physics of the Earth and Planetary Interiors, 68, 9–31.

Masursky, H., 1964. A preliminary report on the role of isostatic rebound in the geologic development of the lunar crater Ptolemaeus, in Astrogeologic Studies, Annu. Prog. Rep., A, pp. 102–134, U.S. Geol. Surv, Washington, D. C.

Mathieu, L., van Wyk de Vries, B., Holohan, E.P., Troll, V.R., 2008. Dykes, cups, saucers and sills: Analogue experiments on magma intrusion into brittle rocks. Earth and Planetary Science Letters 271, 1–13, doi:10.1016/j.epsl.2008.02.020

Menand, T., 2008. The mechanics and dynamics of sills in layered elastic rocks and their implications for the growth of laccoliths and other igneous complexes. Earth and Planetary Science Letters 267, 93–99, doi:10.1016/j.epsl.2007.11.043

Menand, T., 2011. Physical controls and depth of emplacement of igneous bodies: A review. Tectonophysics 500, 11–19, doi:10.1016/j.tecto.2009.10.016

Michaut, C., 2011. Dynamics of magmatic intrusions in the upper crust: Theory and applications to laccoliths on Earth and the Moon, J. Geophys. Res., 116, B05205, doi:10.1029/2010JB008108

Muller, O.H., Muller, M.R., 1980. Near surface magma movement. Proc. Lunar Planet Sci. Conf. 11th, pp. 1979-1985. Pergamon Press, New York.

Newcombe, M.E., Brett, A., Beckett, J.R., Baker, M.B., Newman, S., Guan, Y., Eiler, J.M., Stolper, E.M., 2017. Solubility of water in lunar basalt at low pH_2O. Geochim. Cosmochim. Acta. 200, 330–352.

Orphal, D.L., 1979. Depth, thickness and volume of the breccia lens for simple explosion and impact craters. Lunar and Planetary Science X, abstract #1333.

Pike, R.J., 1980. Geometric interpretation of lunar craters. U.S. Geol. Surv. Prof. Paper, 1046-C, pp. C1–C77.

Pollard, D.P., Johnson, A. M., 1973. Mechanics of growth of some laccolithic intrusions in the Henry Mountains, Utah. II. Bending and failure of overburden layers and sill formation. Tectonophysics, 18, 311–354.

Pollard, D.D., Muller, O.H., Dockstader, D.R., 1975. Form and growth of fingered sheet intrusions. Geological Society of America Bulletin, 86, 351–363.

Roberts, J.L., 1970. The intrusion of magma into brittle rocks. In: Newall, G., Rast, N. (eds) Mechanism of igneous intrusion. Geological Journal Special Issue 2, 287–338.

Robinson, M.S., Brylow, S.M., Tschimmel, M. et al., 2010, Lunar Reconnaissance Orbiter Camera (LROC) instrument overview, Space Sci. Rev. 150, 81-124. doi 10:1007/s11214-010-9634-2.

Roy, R.F., Beck, A.E., Touloukian, Y.S., 1981. Thermophysical properties of rocks. In: Y.S. Touloukian, W.R. Judd and R.F. Roy (Editors), Physical Properties of Rocks and Minerals. McGraw-Hill, New York, 409-502.

Rubin, A.M., 1990. A comparison of rift-zone tectonics in Iceland and Hawaii. Bull. Volcanol. 52, 302–319.

Rubin, A.M., 1993. Dikes vs. diapirs in viscoelastic rock. Earth Planet. Sci. Lett. 119, 641-659.

Rubin, A.M., 1995. Propagation of magma-filled cracks. Annual Review of Earth and Planetary Sciences 23, 287–336.

Rubin, A.M., Pollard, D. D., 1987. Origins of blade-like dikes in volcanic rift zones, in Volcanism in Hawaii, edited by R. W. Decker, T. L. Wright, and P. H. Stauffer, U.S. Geol. Surv. Prof. Pap. 1350, 1449–1470.

Rutherford, M. J., Head, J. W., Saal, A. E., Hauri, E, Wilson, L., 2017. Model for the origin, ascent and eruption of lunar picritic magmas. Am. Mineralogist, 10.2138/am-2017-5994.

Sato, M., 1976. Oxygen fugacity and other thermochemical parameters of Apollo 17 high-Ti basalts and their implications on the reduction mechanism. Proceeding of the 7th Lunar Planetary Science Conference, 1323–1344.

Schofield, N., Stevenson, C., Reston, T., 2010. Magma fingers and host rock fluidization in the emplacement of sills. Geology, 38, 63–66.

Schofield, N.J., Brown, D.J., Magee, C., Stevenson, C.T., 2012. Sill morphology and comparison of brittle and non-brittle emplacement mechanisms. Journal of the Geological Society, London 169, 127–141, doi: 10.1144/0016-76492011-078.

Schultz, P. H., 1976. Floor-fractured lunar craters. Moon, 15, 241–273, doi:10.1007/BF00562240.

Smith, D.E., Zuber, M.T., Neumann, G.A., et al., 2010. Initial observations from the Lunar Orbiter Laser Altimeter (LOLA). Geophys. Res. Lett. 37, L18204, doi 10:1029/2010GL043751.

Soderblom, J.M., Evans, A.J., Johnson, B.C., Melosh, H.J., Miljković, K., Phillips, R.J., Andrews-Hanna, J.C., Bierson, C.J., Head, J.W., Milbury, C., Neumann, G.A., Nimmo, F., Smith, D.E., Solomon, S.C., Sori, M.M., Wieczorek, M.A., Zuber, M.T., 2015. Geophysical Research Letters, 42, 6939–6944, doi:10.1002/2015GL065022

Sparks, R.S.J., 1978. The dynamics of bubble formation and growth in magmas: A review and analysis. Journal of Volcanology and Geothermal Research, 3, 1–37.

Thomson, K., 2007. Determining magma flow in sills, dykes and laccoliths and their implications for sill emplacement mechanisms. Bulletin of Volcanology 70, 183–201, doi:10.1007/s00445-007-0131-8

Thorey, C., Michaut, C., 2014. A model for the dynamics of crater-centered intrusion: Application to lunar floor-fractured craters. J. Geophys. Res. Planets, 119, 286–312, doi:10.1002/2013JE004467

Turcotte, D.L., Schubert, G., 2002. Geodynamics. Cambridge Univ. Press, 275 pp .

Weertman, J., 1971. Theory of water-filled crevasses in glaciers applied to vertical magma transport beneath oceanic ridges. J. Geophys. Res. 76, 1171-1183.

Wichman, R. W., Schultz, P. H., 1995. Floor-fractured craters in Mare Smythii and west of Oceanus Procellarum Implications of crater modification by viscous relaxation and igneous intrusion models. J. Geophys. Res., 100, 21,209–21,218.

Wichman, R. W., Schultz, P. H., 1996. Crater-centered laccoliths on the Moon: Modeling intrusion depth and magmatic pressure at the crater Taruntius. Icarus, 122, 193–199, doi:10.1006/icar.1996.0118.

Wieczorek, M.A., Neumann, G.A., Nimmo, F., Kiefer, W.S., Taylor, G.J., Melosh, H.J., Phillips, R.J., Solomon, S.C., Andrews-Hanna, J.C., Asmar, S.W., Konopliv, A.S., Lemoine, F.G., Smith, D.E., Watkins, M.M., Williams, J.G., Zuber, M.T., 2013. The crust of the Moon as seen on GRAIL. Science 339, 671–675, doi: 10.1126/science.1231530.

Wilson, L., Head, J.W., 2003, Deep generation of magmatic gas on the Moon and implications for pyroclastic eruptions, Geophys. Res. Lett., 30 (12), 1605, doi: 10.1029/2002GL016082.

Wilson, L., Head, J.W., 2017a. Generation, ascent and eruption of magma on the Moon: new insights into source depths, magma supply, intrusions and effusive/explosive eruptions (Part 1: Theory). Icarus, 283, 146–175, doi:/10.1016/j.icarus.2015.12.039.

Wilson, L., Head, J.W., 2017b. Eruption of Magmatic Foams on the Moon: Formation in the Waning Stages of Dike Emplacement Events as an Explanation of "Irregular Mare Patches", Journal of Volcanology and Geothermal Research, 335C, 113–127, 10.1016/j.jvolgeores.2017.02.009

(a)

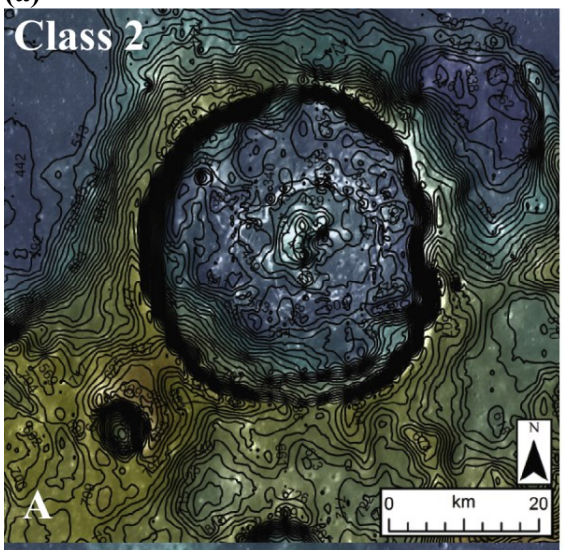

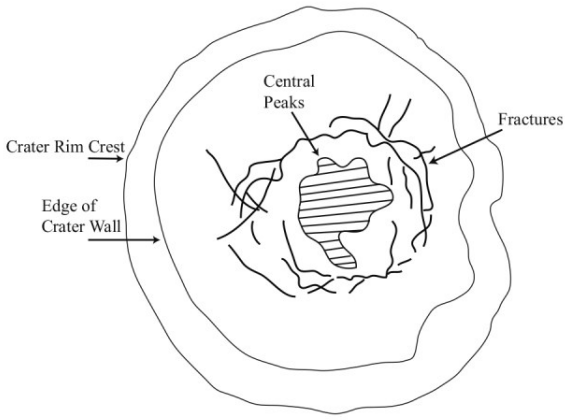

B

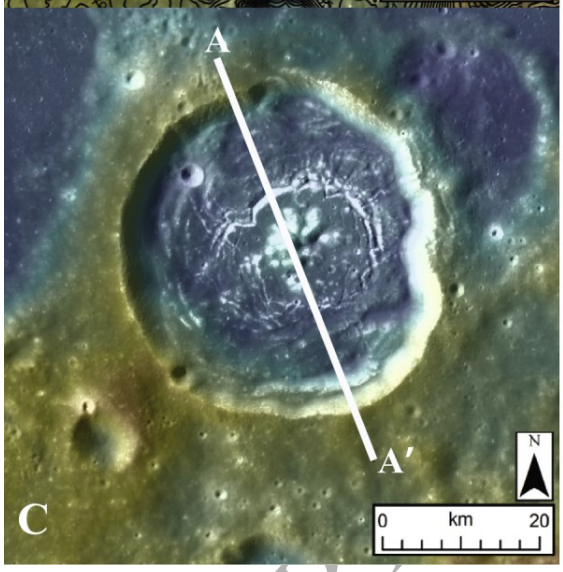

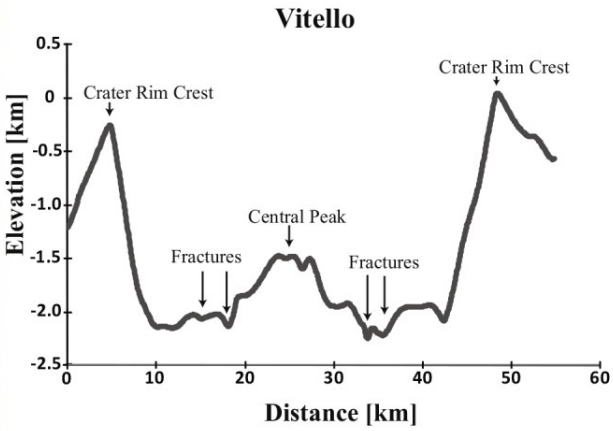

D

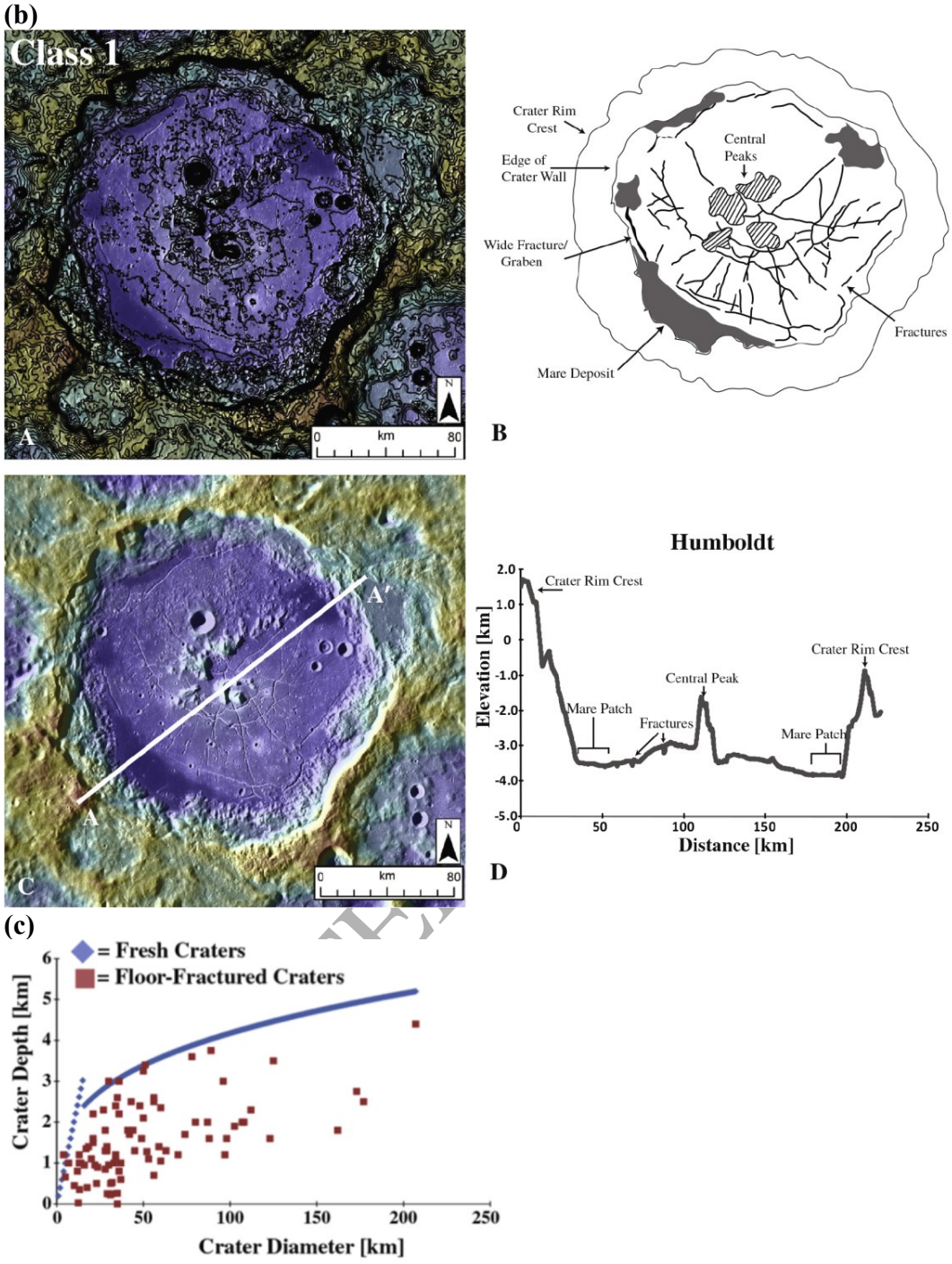

Figure 1. Floor-fractured craters:

a) The crater Vitello, 44 km in diameter (30.4S, 37.5W), a Class 2 floor-fractured crater (Schultz, 1976; Jozwiak et al., 2015). (A) Topographic contour map with 100 m contour intervals on a color-coded altimetry map (blue low, red high) on LROC-WAC image data (Robinson et al., 2010). (B) Geologic sketch map: the most prominent features of Vitello are the numerous concentric fractures surrounding the uplifted central peak region. (C) LOLA gridded topographic data (512 px/deg) overlain with LROC-WAC image data for Vitello showing the location of the

topographic profile shown in (D). (D) Topographic profile
of the crater Vitello showing the raised and upbowed floor relative to fresh craters of this diameter. LOLA altimetry data (Smith et al., 2010).
b) The crater Humboldt, 207 km in diameter (27.2S, 80.9E), a Class 1 floor-fractured crater (Schultz, 1976; Jozwiak et al., 2015). (A) Topographic contour map with 250 m contour intervals on a color-coded altimetry map (blue low, red high). (B) Geologic sketch map: The most prominent morphologic features in Humboldt are the complex of radial and concentric fractures and the wall-adjacent patches of mare material. LROC-WAC image data. (C) LOLA gridded topographic data (512 px/deg) overlain with LROC-WAC image data for Humboldt showing the location of the topographic profile shown in (D). (D) Topographic profile of the crater Humboldt showing similar characteristics to those in (B). LOLA altimetry data.
c) Depth to diameter relationship for lunar floor-fractured craters (FFCs) (red squares) compared with the idealized depth to diameter ratio for unmodified craters of identical diameter (blue diamonds and blue line), calculated using the equations of Pike (1980) for simple craters (D < 15 km) and complex craters (D > 15 km). The population of FFCs shows significantly shallower floors than would be predicted given their equivalent fresh-crater diameter. From Jozwiak et al. (2015)

(**a**)

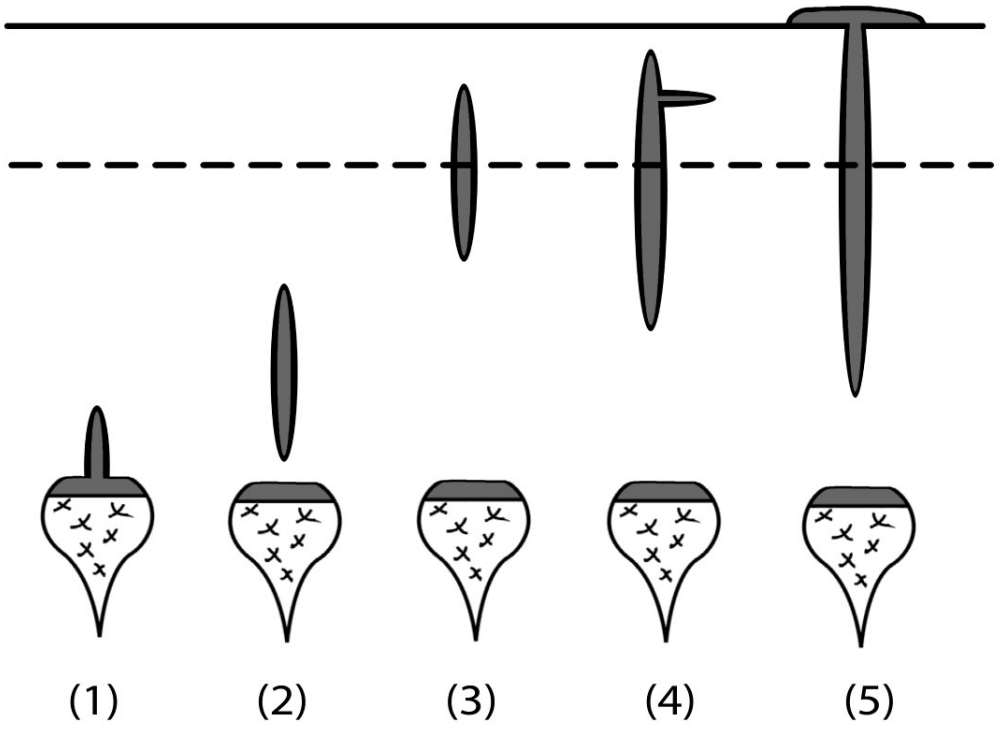

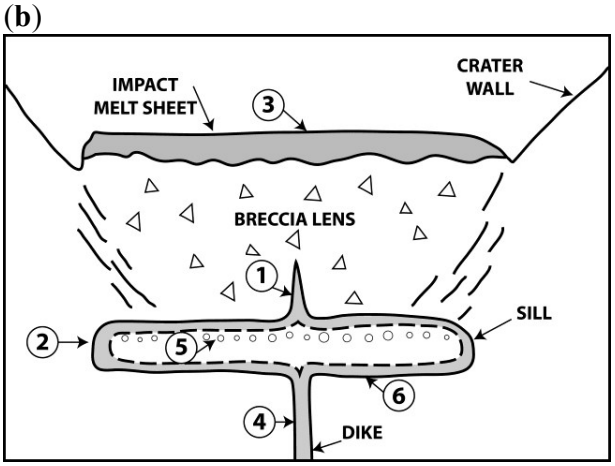

Figure 2. Magmatic intrusion.
a) Proposed scenario for origin of magma reaching the surface or shallow intrusions on the Moon. (1) a dike grows from a partial melt zone; (2) the dike pinches off from its source and migrates as an isolated structure; (3) the dike attempts to stabilize at the crust-mantle interface where it is neutrally buoyant, and may stall as an intruded dike, or (4) feed a shallow sill, or (5) cause a surface eruption.
b) Cross-sectional diagram of intrusion. (1) Initially, a dike intrudes into the breccia lens below the preexisting crater floor, and slightly overshoots the rheological discontinuity at the base of the ductile breccia lens; (2) excess pressure in the dike causes the sill to then spread laterally and grow vertically, uplifting the crater floor (3), and deforming and fracturing the rigid impact melt sheet lining the crater floor; (4) sill formation and floor uplift continue until the excess pressure in the underlying dike equilibrates; (5) intruded magma in the sill undergoes volatile evolution, causing formation of a foam layer and its collapse; (6) intruded sill magma undergoes final cooling, shrinkage and subsidence until solidified, resulting in a net subsidence of ~10%.

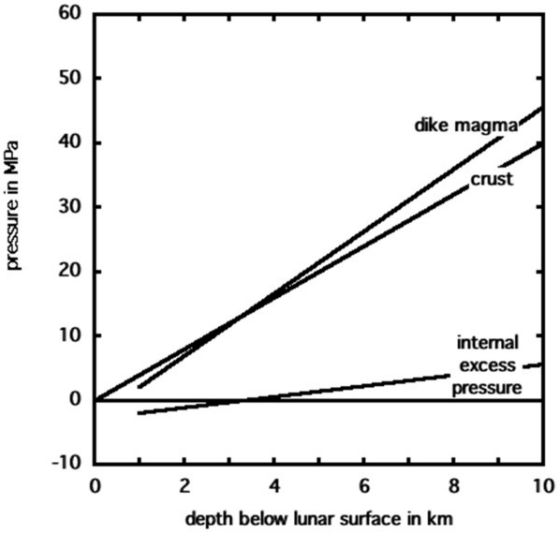

Figure 3. Variation with depth below the lunar surface of the total pressure in a dike, the lithostatic stress due to the weight of the crust, and the excess pressure in the dike magma. The dike top is 1 km below the lunar surface, and the pressure gradient in the dike magma is assumed to be uniform.

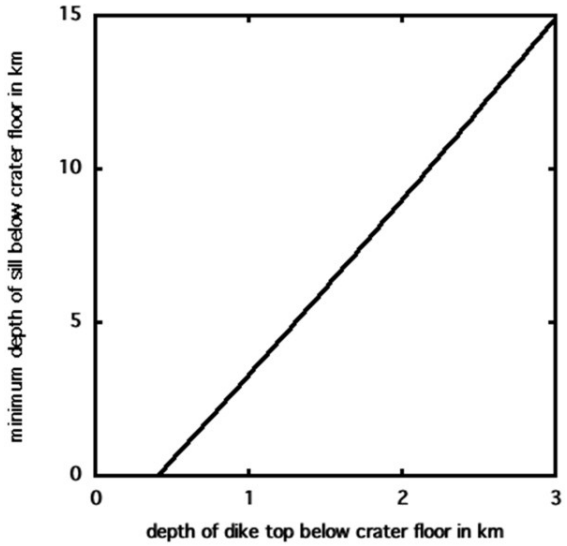

Figure 4. Variation of the minimum depth at which a sill can be initiated by a dike as a function of the depth of the dike top below the lunar surface. The pressure gradient in the dike magma is assumed to be uniform.

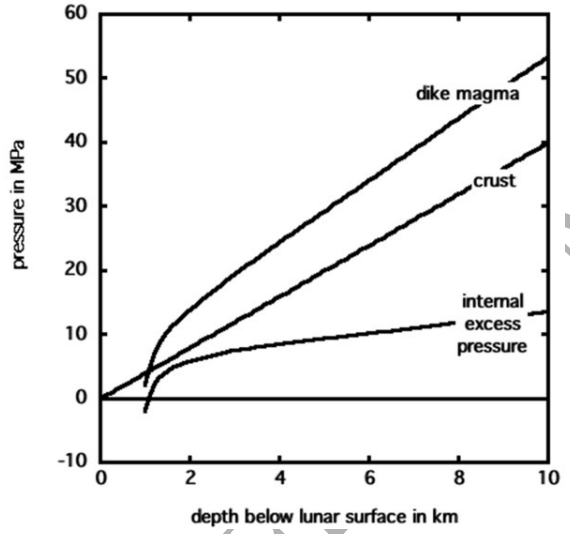

Figure 5. Variation with depth below the lunar surface of the total pressure in a dike, the lithostatic stress due to the weight of the crust, and the excess pressure in the dike magma. The dike top is 1 km below the lunar surface, and the pressure gradient in the dike magma is assumed to be variable with depth, being greatest near the dike tip.

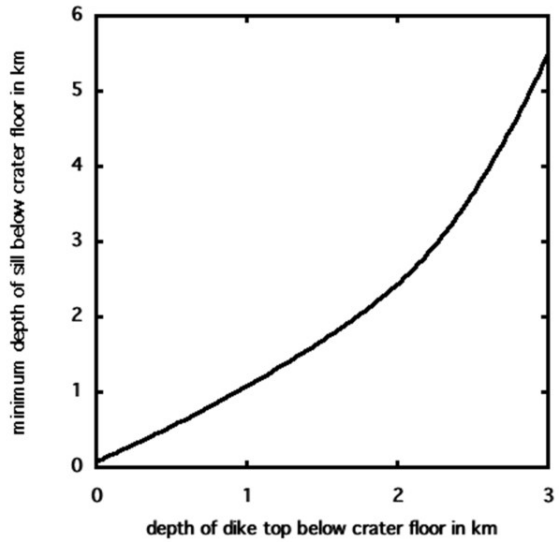

Figure 6. Variation of the minimum depth at which a sill can be initiated by a dike as a function of the depth of the dike top below the lunar surface. The pressure gradient in the dike magma is assumed to be variable with depth, being greatest near the dike tip.

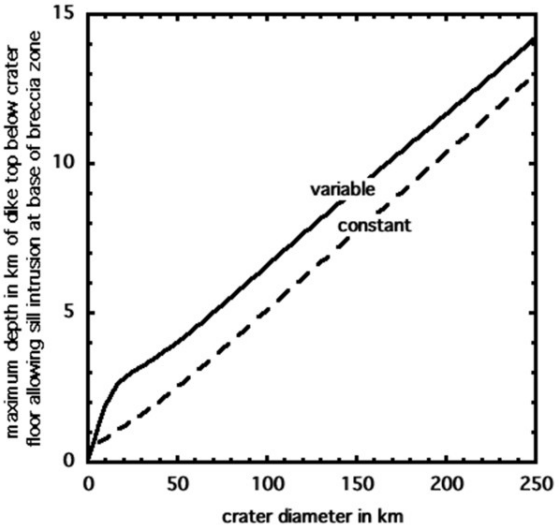

Figure 7. Variation with impact crater diameter of the maximum depth of the dike top below the crater floor that allows a sill to be intruded at the base of the breccia zone beneath an impact crater. Curves are shown for both constant and variable dike magma pressure gradients.

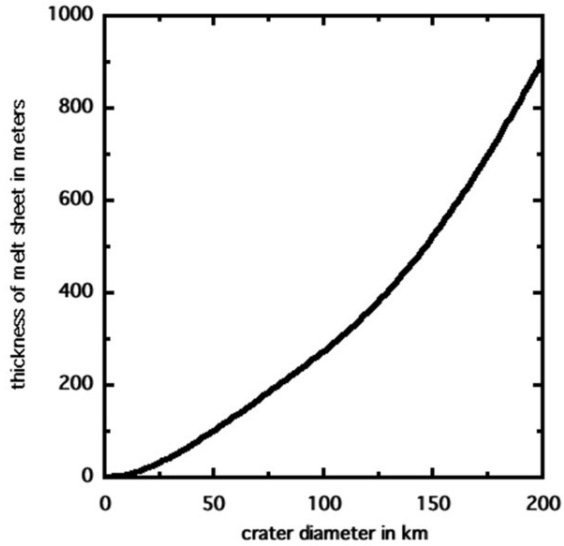

Figure 8. Variation with impact crater diameter of the expected thickness of an impact melt sheet on the crater floor.

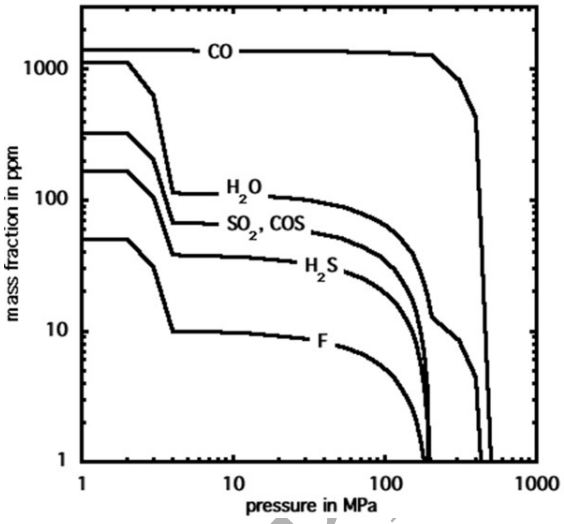

Figure 9. Variation with pressure of the amounts of volatiles released from an ascending lunar magma. Curves are labelled by the relevant species; the breaks in slope are due to the interpolation method used.

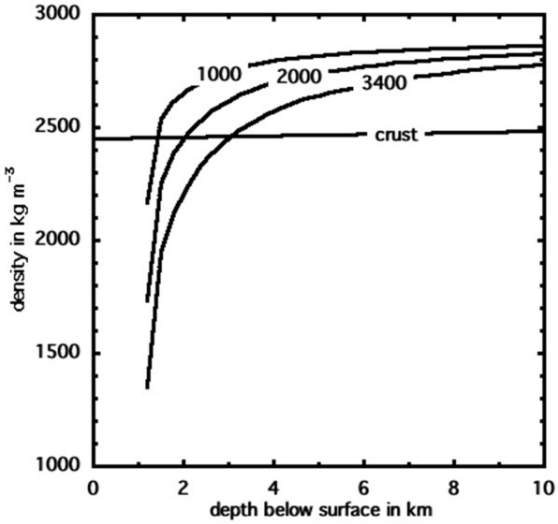

Figure 10. Variation with depth below the lunar surface of the density of the crust and of the bulk density of the magma in a dike that has its upper tip 1 km below the surface. Curves are labelled by the total amount in ppm of all volatiles released. The pressure gradient in the dike magma is assumed to be uniform.

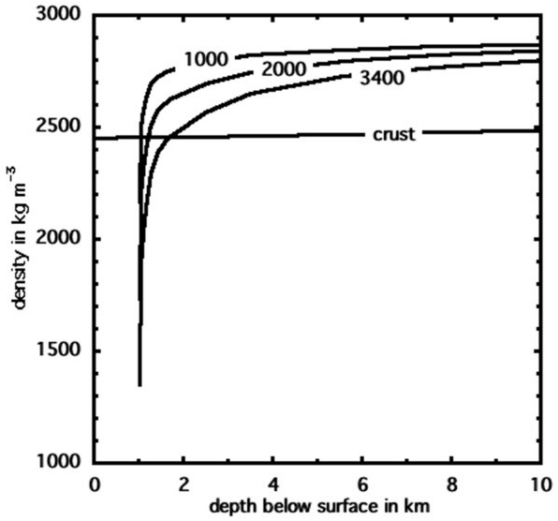

Figure 11. Variation with depth below the lunar surface of the density of the crust and of the bulk density of the magma in a dike that has its upper tip 1 km below the surface. Curves are labelled by the total amount in ppm of all volatiles released. The pressure gradient in the dike magma is assumed to be variable with depth, being greatest near the dike tip.

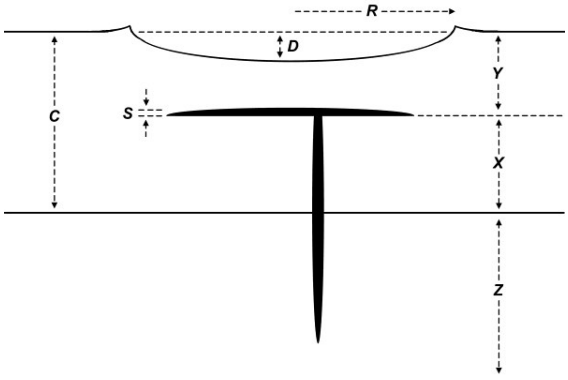

Figure 12. The configuration of a dike that has failed to erupt at the surface and instead has formed a sill in the breccia lens beneath an impact crater. The crust-mantle boundary is at depth *C* below the surface.

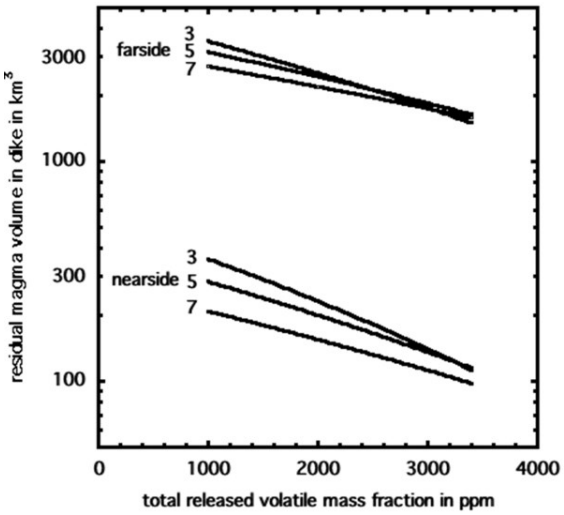

Figure 13. Variation with total released magma volatile amount of the residual magma volume in a dike feeding a sill beneath a floor-fractured crater. Three sill intrusion depths, 3, 5 and 7 km, are shown for each of the nearside and the farside.

(**a**)

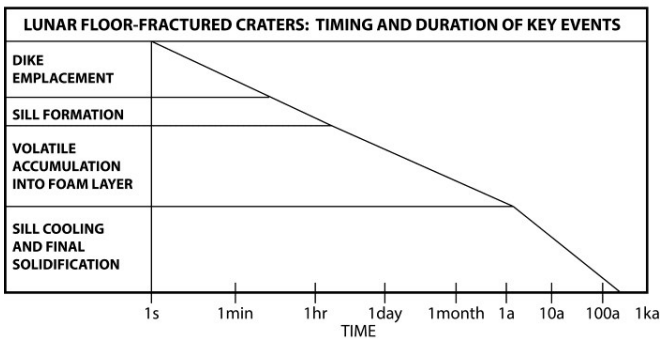

(**b**)

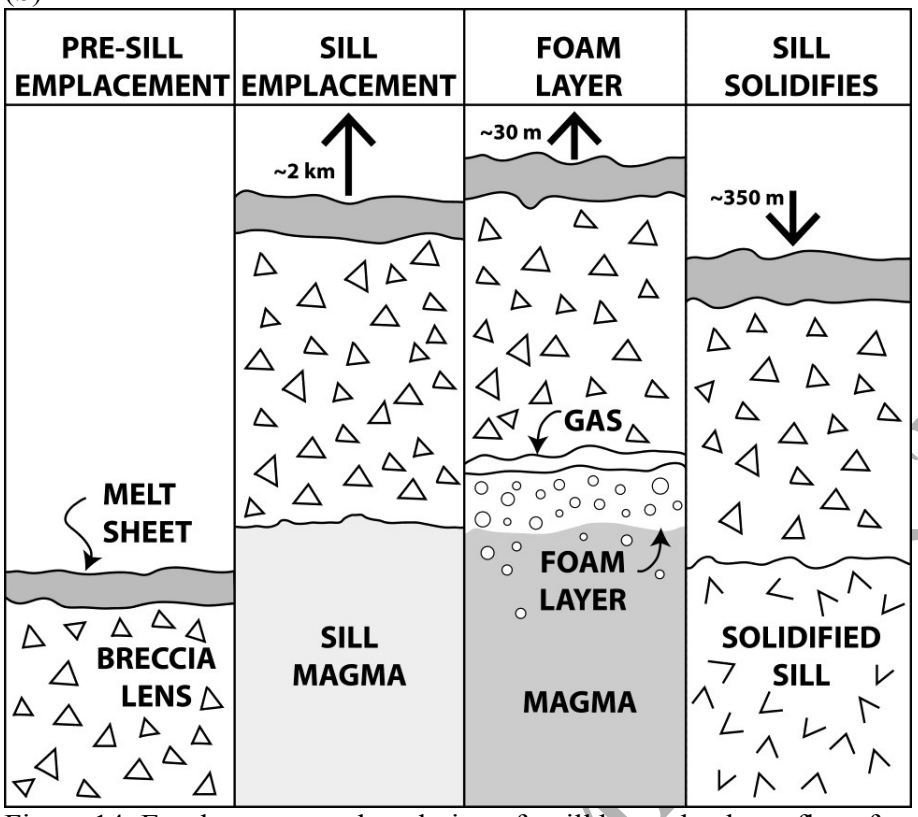

Figure 14: Emplacement and evolution of a sill beneath a large floor-fractured crater:
a) Timeline for major events in the emplacement and evolution of a sill beneath a large floor-fractured crater. The dike emplacement and sill intrusion events are very rapid compared with the time needed for sill volatile evolution, and magma cooling until sill solidification. Time is in a log scale.
b) Diagrammatic representation of the changes in floor elevation in a large floor-fractured crater intruded by a sill. a) Pre-sill intrusion crater floor; b) sill formation (~2 km thick in this case) causes floor uplift; c) volatile segregation causes additional sill thickening and potential floor uplift (~30 m); d) cooling and solidification causes sill shrinkage and thickness reduction (~350 m), potentially manifested in crater floor deformation. Final crater floor surface above completely cooled ~2 km thick intruded sill should be ~320 m below initial sill intrusion and uplift elevation (+2 km intrusion, +30 m from foam/gas layer, -350 m from cooling and solidification).

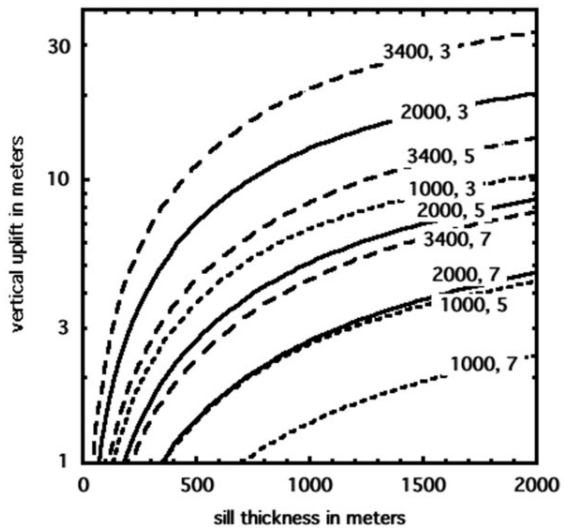

Figure 15. Variation of the uplift, *U*, of the overlying strata with initial sill thickness, *S*, for total magma volatile amounts of 1000, 2000 and 3400 ppm and sill intrusion depths of 3, 5 and 7 km.

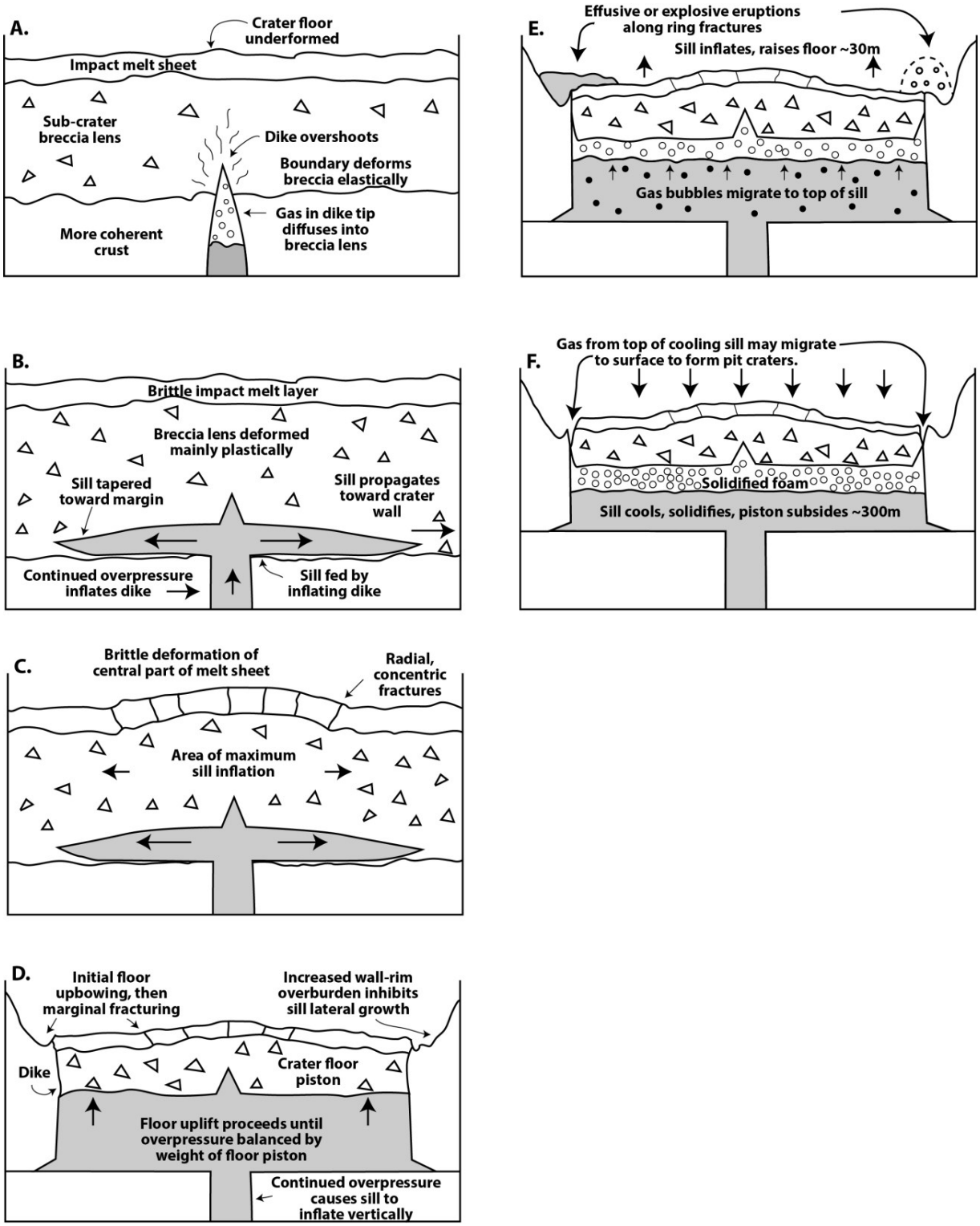

Figure 16. Framework for the predicted behavior of surface deformational and volcanic processes arising from a dike and sill intrusion beneath an impact crater.

a) Initially, a dike intrudes beneath an impact crater and stalls several kilometers below the crater floor at the zone of physical properties transition between the more coherent highlands substrate

and the less coherent sub-crater breccia lens, typically overshooting this zone by several hundred meters. Depth of dike tip below the crater floor must be greater than at least a few hundred meters, otherwise an effusive eruption is likely to occur, rather than a sill intrusion. Lack of a distinctive linear graben on most FFC floors also supports a depth in excess of hundreds of meters to a few kilometers (Head and Wilson, 1994). Deformation of the lower-density breccia lens by the top of the dike should be elastic, and the overlying solidified impact melt sheet on the crater floor is predicted to be undeformed. Gas in the dike tip (Wilson and Head, 2003) is predicted to diffuse into the breccia zone or under some circumstances propagate a minor crack to the surface and vent.

b/c) Continued overpressure from the buoyant magma remaining in the part of the dike extending into the mantle causes the dike to inflate at the rheological boundary and begin to feed a sill that propagates laterally until it reaches supply limitation, pressure equilibration, or the base of the wall at the edge of the floor where the crater rim/wall overburden causes the sill to cease lateral migration (Thorey and Michaut, 2014). The exact shape of the growing sill is dependent on 1) the location of the dike relative to the crater floor, 2) the location of the top of the dike (see Figure 17), and 3) the size of the crater floor (small crater floors transition to the piston-uplift stage more rapidly, while very large crater floors may host supply-limited sills). In this diagram we assume a crater-centered intrusion (Figure 17, upper left). In cross-section, the growing sill is tapered from its contact with the dike outward toward its propagating tip. Lateral and vertical sill growth deform the overlying breccia lens mainly plastically; deformation of the brittle crater floor impact-melt layer may occur over the area of maximum sill inflation (center) if the breccia lens undergoes sufficient elastic deformation (c). In this case (c), the central part of the crater floor melt sheet might deform in a brittle manner due to the hinge-like upbowing attributed to the tapered growth of the sill, and radial and concentric fractures might ensue, depending on the magnitude and balance of sill-induced stresses.

d) As the propagating sill reaches the margins of the crater floor (very rapidly, in a few hours; Figure 14b) and the increased rim/wall overburden inhibits the sill from further lateral propagation, continued overpressure cause the sill to inflate vertically, inducing initial floor upbowing depending on the plastic response of the overlying breccia lens and the elastic response of the impact melt sheet. Eventually, inflation–induced stresses at the top of the sill cause fracturing at the margins of the sill (edge of the crater floor) and piston-like uplift of the crater floor. The inflating sill upbows the crater floor until the marginal fractures occur; the stress gradient then disappears and uplift of the crater floor proceeds until the dike emplacement overpressures are balanced by the weight of the piston-like crater floor overlying the growing sill. Because sill emplacement and floor uplift occur in less than a few hours (Figure 14b), maximum bubble collection and foam growth has not yet occurred. These two factors lead to the prediction that at this stage, magma will rise along the peripheral fractures of the piston to form ring-dike-like intrusions, but will not rise to the surface to form eruptions because of the isostatic nature of the system; the isostatic nature predicts that dikes will rise in the peripheral faults to the same level as that to which the initial dike tip was emplaced. However, if there is sufficient exsolved gas in the magma in these dikes remaining from the emplacement stage, then it is possible that volatile-assisted buoyancy might result in effusive, and perhaps pyroclastic-associated, eruptions. Ultimately, the floor is uplifted by as much as ~3 kilometers above its original position; we assume about 2 km in this case.

e) In the period of time following initial piston-like floor uplift (Figure 14b), gas bubbles rise in the intruded sill, forming a foam layer at the top of the sill over the course of several months.

The increase in volume caused by gas exsolution and expansion cause the sill to inflate by a height of ~30 m, creating upward stresses in the breccia lens and crater floor. The combination of increase pressure in the sill, modest floor uplift, and available gas bubbles in the magma, combine to optimize the likelihood that magma will now be buoyant in the ring-fracture dikes and that it will erupt onto the crater floor. Eruptive options include a) an effusive eruption accompanied by pyroclastic activity, b) a foam-rich Hawaiian eruption, or c) if the previous dike has solidified at the top, a vulcanian eruption (Head and Wilson, 1979) driven by gas pressure build-up. Subsequently, once the critical stable depth of a foam layer of ~15 m is exceeded, the magma in the foam bubble walls will drain back into the sill and eventually produce a gas layer overlying a residual foam layer. The ~30 m additional uplift of the crater floor may also induce brittle deformation in the melt sheet cap and perhaps result in venting of the foam and/or gas along old or new fractures. Alternatively, the ~15 m of foam will cool and solidify as part of the overall sill. In any case, pyroclastic eruptions should be favored in smaller craters, where the initial dikes are shallower and the excess pressures are proportionally greater than the lithostatic loads due to the overburdens.

f) In the final stage, the intruded sill undergoes cooling over a period of the order of decades to centuries, resulting in contraction of the volume of the sill and subsidence of the crater floor by ~350 m. As the sill progressively solidifies, there is less and less likelihood that magma from the sill will erupt, but due to the contraction and modest sinking of the floor and piston-like plug, gas from the top of the cooling sill may migrate to the surface along cracks and cause gas eruptions to form pit craters with fragmental regolith ejecta deposits, or drainage of regolith into the breccia lens below to form collapse pits. Disaggregated foam is unlikely to accompany these later eruptions as the foam should have solidified early in the cooling phase at the top of the sill.

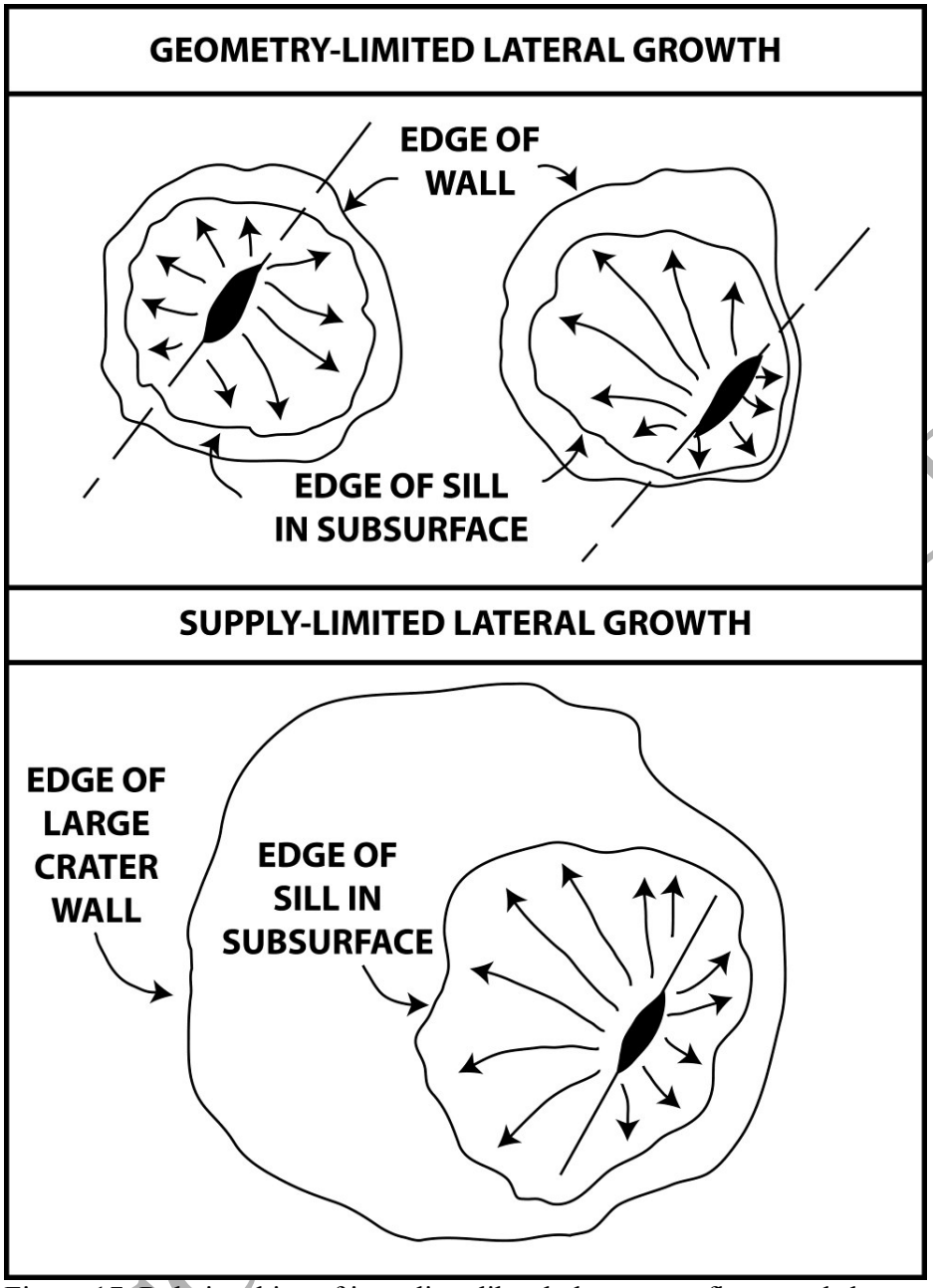

Figure 17. Relationships of intruding dikes below crater floors and shapes of sill intrusions. Top: Geometry-limited lateral growth: In these two cases, dikes intrude below the crater floor and spread laterally from the widest part in the dike to form a sill, whose lateral extent is determined by the overburden pressure of the crater wall and rim (outer circle). In the left example, the strike of the dike intersects the center of the crater floor, and the top of the dike is also in the center, and the sill spreads symmetrically. In the right example, the dike intrudes below the edge of the crater floor and the sill intrudes and spreads laterally to the far crater wall. Inhibition of lateral spreading in both cases forces sill inflation and uplift of the crater floor. Bottom: Supply-limited lateral growth: In this case the crater diameter and floor diameter are large compared to the volume of magma available to form a spreading sill and the sill extent is constrained on the southeast by the crater wall and rim, and constrained elsewhere below the crater floor by the total

supply of available magma. Each of these three options carries specific predictions about the sequence and scale of associated FFC floor deformation and possible volcanic venting.

Table 1. For isolated dikes approaching the surface from mantle depths on the nearside of the Moon, values are given for the vertical length, L, the total magma volume, V, the average value of the total pressure gradient in the dike magma, P_t', and the average value of the pressure gradient driving magma flow, P_f'.

L / km	V / km^3	P_t' / (Pa m^{-1})	P_f' / (Pa m^{-1})
47.1	70.6	4841.2	143.2
52.1	105.5	4845.2	147.2
62.8	223.1	4851.8	153.8
78.5	544.6	4858.2	160.2
85.0	748.6	4860.2	162.2
94.2	1129.4	4862.4	164.4

Table 2. Residual dike volumes for intrusions in the C = 30 km thick nearside lunar crust. All entries are for sills intruded at depth Y = 5 km below the lunar surface so that the extent of the residual dike above the crust-mantle boundary is X = 25 km, resulting in P_c = 19.9 MPa and ρ_c = 2508 kg m^{-3}. Each part of the table relates to a different total amount of volatiles, n, released from the magma. The tabulated values show the variation with sill thickness, S, of the final extent of the dike below the crust-mantle boundary, Z, the excess pressure at the crust-mantle boundary holding the dike open, P_e, the mean width of the dike, W, and the volume of magma remaining in it after the intrusion has formed, V. The mean values of Z, P_e, W and V are also shown.

(a) n = 1000 ppm, ρ_{lc} = 2859 kg m^{-3} and ρ_{lm} = 2892 kg m^{-3}				
S	Z	P_e	W	V
/km	/km	/MPa	/m	/km^3
0.1	23.9	14.3	136.0	255.7
0.5	24.3	14.5	140.2	267.8
1	24.8	14.8	145.5	283.4
2	25.8	15.4	156.3	316.1
	24.7 ± 0.7	14.7 ± 0.4	144.5 ± 7.6	280.7 ± 22.6
(b) n = 2000 ppm, ρ_{lc} = 2820 kg m^{-3} and ρ_{lm} = 2885 kg m^{-3}				
S	Z	P_e	W	V
/km	/km	/MPa	/m	/km^3
0.1	20.9	12.7	109.6	179.8
0.5	21.2	12.9	113.1	188.4
1	21.6	13.1	117.4	199.5
2	21.9	13.6	123.9	212.9
	21.4 ± 0.4	13.1 ± 0.4	1146.0 ± 5.3	195.2 ± 12.4
(c) n = 3400 ppm, ρ_{lc} = 2767 kg m^{-3} and ρ_{lm} = 2875 kg m^{-3}				

S	Z	P_e	W	V
/km	/km	/MPa	/m	/km^3
0.1	16.9	10.5	78.0	103.5
0.5	17.2	10.7	80.5	108.5
1	17.5	10.9	83.7	115.0
2	18.2	11.3	90.1	128.6
	17.4 ± 0.5	10.9 ± 0.3	83.1 ± 4.5	113.9 ± 9.4

Table 3. Residual dike volumes for intrusions in the C = 50 km thick farside lunar crust. All entries are for sills intruded at depth Y = 5 km below the lunar surface so that the extent of the residual dike above the crust-mantle boundary is X = 45 km, resulting in P_c = 19.9 MPa and ρ_c = 2505 kg m^{-3}. Each part of the table relates to a different total amount of volatiles, n, released from the magma. The tabulated values show the variation with sill thickness, S, of the final extent of the dike below the crust-mantle boundary, Z, the excess pressure at the crust-mantle boundary holding the dike open, P_e, the mean width of the dike, W, and the volume of magma remaining in it after the intrusion has formed, V. The mean values of Z, P_e, W and V are also shown.

(a) n = 1000 ppm, ρ_{lc} = 2866 kg m^{-3} and ρ_{lm} = 2898 kg m^{-3}				
S	Z	P_e	W	V
/km	/km	/MPa	/m	/km^3
0.1	45.0	26.4	466.1	2963.8
0.5	45.4	26.6	474.1	3041.1
1	45.9	26.9	484.1	3139.4
2	46.9	27.5	504.3	3341.6
	45.8 ± 0.7	26.8 ± 0.4	482.2 ± 14.3	3121.4 ± 141.5
(b) n = 2000 ppm, ρ_{lc} = 2834 kg m^{-3} and ρ_{lm} = 2897 kg m^{-3}				
S	Z	P_e	W	V
/km	/km	/MPa	/m	/km^3
0.1	40.87	24.03	396.70	2291.89
0.5	41.23	24.24	403.54	2352.08
1	41.68	24.51	412.14	2428.61
2	42.59	25.04	429.52	2586.00
	41.6 ± 0.6	24.5 ± 0.4	410.5 ± 12.3	2414.6 ± 110.2
(c) n = 3400 ppm, ρ_{lc} = 2790 kg m^{-3} and ρ_{lm} = 2895 kg m^{-3}				
S	Z	P_e	W	V
/km	/km	/MPa	/m	/km^3
0.1	35.2	20.8	309.3	1541.0
0.5	35.6	21.0	314.7	1581.9
1	35.9	21.3	321.5	1634.0
2	36.7	21.7	335.3	1741.0
	35.9 ± 0.6	21.2 ± 0.3	320.2 ± 9.7	1624.5 ± 74.9